Draft version July 14, 2021
Typeset using LATEX twocolumn style in AASTeX631

Type Icn SN 2021csp, the Origins of the Fastest Supernovae, and the Fates of Wolf-Rayet Stars

Daniel A. Perley,[1] Jesper Sollerman,[2] Steve Schulze,[2] Yuhan Yao,[3] Christoffer Fremling,[3] Avishay Gal-Yam,[4] Anna Y. Q. Ho,[5,6] Yi Yang,[5] Erik C. Kool,[2] Ido Irani,[4] Lin Yan,[7] Dietrich Baade,[8] Eric C. Bellm,[9] Thomas G. Brink,[5] Ting-Wan Chen,[2] Aleksandar Cikota,[8,10] Aishwarya Dahiwale,[3] Richard Dekany,[7] Dmitry A. Duev,[3] Alexei V. Filippenko,[5] Peter Hoeflich,[11] Mansi M. Kasliwal,[3] S. R. Kulkarni,[3] Ragnhild Lunnan,[2] Frank J. Masci,[12] Justyn R. Maund,[13] Reed Riddle,[7] Philippe Rosnet,[14] David L. Shupe,[12] Nora Strotjohann,[4] Anastasios Tzanidakis,[3] and Stefan van der Walt[5]

[1] *Astrophysics Research Institute, Liverpool John Moores University, IC2, Liverpool Science Park, 146 Brownlow Hill, Liverpool L3 5RF, UK*
[2] *The Oskar Klein Centre, Department of Astronomy and Department of Physics, Stockholm University, AlbaNova, SE-106 91 Stockholm, Sweden*
[3] *Division of Physics, Mathematics, and Astronomy, California Institute of Technology, Pasadena, CA 91125, USA*
[4] *Department of Particle Physics and Astrophysics, Weizmann Institute of Science, 76100 Rehovot, Israel*
[5] *Department of Astronomy, University of California, Berkeley, CA 94720-3411, USA*
[6] *Miller Institute for Basic Research in Science, University of California, Berkeley, CA 94720, USA*
[7] *Caltech Optical Observatories, California Institute of Technology, Pasadena, CA 91125, USA*
[8] *European Southern Observatory, Karl-Schwarzschild-Str. 2, 85748 Garching b. München, Germany*
[9] *DIRAC Institute, Department of Astronomy, University of Washington, 3910 15th Avenue NE, Seattle, WA 98195, USA*
[10] *Physics Division, Lawrence Berkeley National Laboratory, 1 Cyclotron Road, Berkeley, CA 94720, USA*
[11] *Department of Physics, Florida State University, Tallahassee, Florida 32306-4350, USA*
[12] *IPAC, California Institute of Technology, 1200 E. California Blvd, Pasadena, CA 91125, USA*
[13] *Department of Physics and Astronomy, University of Sheffield, Hicks Building, Hounsfield Road, Sheffield S3 7RH, UK*
[14] *Université Clermont Auvergne, CNRS/IN2P3, LPC, F-63000 Clermont-Ferrand, France*

ABSTRACT

We present an extensive suite of observations of the fast, luminous optical transient SN 2021csp, classifying it as the second member of a new class of supernovae hallmarked by strong, narrow P-Cygni carbon features at early times (a Type Icn supernova). The early evolution of the transient is driven by the strong interaction between very fast SN ejecta ($v \sim 30000$ km s^{-1}) and a massive, dense, fast-moving C/O wind shed by the progenitor—possibly a WC star—a few months before explosion. While the narrow lines disappear after about 10 days and the optical flux fades rapidly after its peak, the transient remains relatively bright for the first 60 days after which the interaction abruptly ceases and the transient vanishes. The lack of a late light curve cobalt tail suggests minimal heavy-element nucleosynthesis and a distinct origin from classical Type Ic supernovae. We place SN 2021csp in context with other fast-evolving transients, and suggest that Type Ibn and Type Icn supernovae, AT2018cow-like fast transients, and other rare hydrogen-poor classes may represent the only visible manifestations of Wolf-Rayet collapse. The rates of these events constitute only a few percent of the predicted death rate of massive Wolf-Rayet stars, suggesting that the vast majority of the WR population collapses to black holes with minimal electromagnetic radiative output. Type Ibn/Icn supernovae may originate when the resulting fast but low-energy fallback supernova interacts with surrounding dense CSM.

Keywords: Supernovae (1668), Core-collapse supernovae (304), Wolf-Rayet Stars (1806), Stellar mass black holes (1611), Transient sources (1851)

d.a.perley@ljmu.ac.uk

1. INTRODUCTION

While progenitor detections, hydrodynamic models, and basic rate calculations all suggest that most single stars born with initial masses between $8-20\ M_\odot$ explode as red supergiants and produce Type IIP supernovae (Smartt 2009), the fates of more massive stars ($> 25\ M_\odot$) remain an open question. Such stars lose a significant fraction of their hydrogen envelopes on the main sequence due to line-driven winds even as single stars (e.g., Vink et al. 2001), and they are also more likely to undergo strong binary interaction (Sana et al. 2012). In either case, a predicted consequence is that many, perhaps most, such stars will be deficient in hydrogen by the time of core collapse. Prior to explosion, such stars will appear as Wolf-Rayet (WR) stars; the explosion itself will then manifest as a supernova of spectroscopic Type IIb, Ib or Ic (a stripped-envelope supernova).

This straightforward picture faces a number of challenges, however. First, hydrodynamic models suggest that the masses ejected in typical Type Ib/c supernovae (SNe) are only a few $M_\odot$, much lower than predicted for exploding WR stars (e.g., Dessart et al. 2012). Second, no WR star has been identified at the site of a SN in pre-explosion imaging: the handful of reported SN Ib/c progenitor candidates are too optically-luminous to be WR stars (Cao et al. 2013; Eldridge & Maund 2016; Kilpatrick et al. 2018, 2021), and upper limits on the remainder are in marginal tension with the luminosity distribution of the Galactic WR population (Eldridge et al. 2013, although c.f. Sander et al. 2019). Third, Type Ib/c SNe are too abundant (by a factor of $\sim$2) to originate solely from the WR population (Smith et al. 2011).

For these reasons, binary evolution involving pairs of lower-mass stars undergoing common-envelope evolution has increasingly been seen as the most likely pathway for explaining most of the Type Ib/c SN population. If so, the final outcome of stellar evolution for more massive stars ($\gtrsim 25\ M_\odot$) remains unclear. One possibility is that very massive stars do not explode at all, and instead collapse directly to black holes with minimal emission of electromagnetic radiation (O'Connor & Ott 2011; Sukhbold & Woosley 2014; Smartt 2015). This remains controversial. Some very massive stars probably explode while still in possession of their hydrogen envelope to produce Type IIn supernovae (Smith et al. 2011; Mauerhan et al. 2013; Smith et al. 2014), although this does not resolve the question of the fates of those massive stars that do undergo a WR phase. Some *atypical* Type Ib/c SNe do appear to be consistent with massive WR progenitors: specifically, about 25% of broad-lined Type Ic (Ic-BL) SNe show ejecta masses consistent with explosions of very massive stars (Taddia et al. 2019), and the progenitors of superluminous supernovae are also likely to be quite massive (Nicholl et al. 2015; Blanchard et al. 2020).

Another rare stripped-envelope SN subtype that has been suggested to be related to very massive stars is the class of Type Ibn SNe. The velocities inferred from the widths of the hallmark narrow lines of these systems (attributed to dense CSM surrounding the progenitor star) are comparable to those seen in Local Group WR stars, suggesting that WR stars may indeed be their progenitors (Foley et al. 2007; Pastorello et al. 2008). However, the pre-explosion mass-loss rates inferred from observations of Type Ibn SNe are much higher than those seen in normal WR winds, implying that any WR progenitor must enter a short-lived evolutionary phase of greatly-enhanced mass loss prior to the explosion.

The list of stripped-envelope SN subtypes continues to expand. Gal-Yam et al. (2021) recently presented a detailed observational study of SN 2019hgp, a fast and luminous transient with no known literature precedent. Early-time spectra of this event are dominated by narrow lines with profiles similar to those seen in Type Ibn SNe but originating from carbon, oxygen, and other alpha elements rather than helium, defining a new class of Type "Icn" supernovae. In their analysis of this object, Gal-Yam et al. (2021) point out that the distinction between Type Ibn and Type Icn SNe closely mirrors that of the WR spectroscopic subtypes (helium/nitrogen-rich WN versus helium-poor, carbon-rich WC stars). On this basis, they postulate that Type Ibn/Icn SNe represent the true outcomes of the explosions of WR stars.

Gal-Yam et al. (2021) also note that the properties of SN 2019hgp (fast-rising, hot, and luminous) show some resemblance to the population of rare, fast-evolving transients identified in photometric surveys (Drout et al. 2014; Tanaka et al. 2016; Pursiainen et al. 2018), sometimes referred to as fast blue optical transients (FBOTs) or rapidly evolving transients (RETs), indicating a possible link with this previously poorly-explored group of objects. However, SN 2019hgp would not itself have been classified as an FBOT/RET by the criteria employed in earlier works.

In this paper we present observations of the second Type Icn supernova to be discovered, SN 2021csp. The properties of this object are qualitatively similar to those of SN 2019hgp but even more extreme. SN 2021csp is faster and more luminous and a far more extensive observational campaign was possible. These observations strengthen the basic model presented by Gal-Yam et al. (2021) but also allow us to further extend it, with important implications for the fates of very massive stars of all types. Indeed, we argue that the distinction between Type Ibn/Icn and "normal" Type Ib/Ic supernovae may involve not only the mass and evolutionary history of the progenitor, but also the nature of the underlying explosion and the type of compact remnant that is left behind.

Our paper is organized as follows. In §2 we present the discovery of SN 2021csp and our extensive observational campaign. In §3 we perform a more detailed analysis of the light curve, spectra, and host galaxy to infer some basic properties of the explosion and pre-explosion system. In §4 we discuss the results of the analysis in the context of the physical nature of the progenitor, its evolutionary state prior to explosion, and the nature of the explosion shock. In §5 we discuss the implications of these results for progenitor models, and in §6 we summarize our conclusions. We use a simple cosmology with $H_0 = 70\,\mathrm{km\,s^{-1}\,Mpc^{-1}}$, Ω_Λ=0.7, $\Omega_M = 0.3$ and reference the times of our observations to an estimated explosion date of MJD 59254.5 (§3.1.1). Apparent magnitudes are reported in the text without an extinction correction, but for subsequent analysis and in our figures we correct for Galactic extinction assuming a reddening of $E(B-V) = 0.027$ mag (Schlafly & Finkbeiner 2011).

2. OBSERVATIONS

2.1. *Palomar 48-inch Discovery and Photometry*

The Zwicky Transient Facility (ZTF; Bellm et al. 2019a; Graham et al. 2019) is a combined public and private time-domain optical sky survey, using a 47 deg^2 field-of-view camera (Dekany et al. 2020) on the refurbished Samuel Oschin 48-inch Schmidt Telescope (P48) at Palomar Observatory. The ZTF observing and alert system are described in previous works (Masci et al. 2019; Patterson et al. 2019; Mahabal et al. 2019; Duev et al. 2019).

SN 2021csp (internally designated ZTF21aakilyd) was first detected in an i-band image obtained on 2021-02-11 as part of the ZTF high-cadence survey (Bellm et al. 2019b) and confirmed with a second observation in g band the same night. The last non-detection was two days prior. It was identified as a candidate of interest the following morning during daily scanning of our custom alert filter (Ho et al. 2020a; Perley et al. 2021b), due to the fast rise (>2.5 mag in two days), blue colors ($g-i = -1$ mag), and coincidence with an extended object (a probable host galaxy), motivating a substantial follow-up campaign (§2.2–2.4).

We used the IPAC forced photometry pipeline to obtain final P48 photometry and pre-explosion upper limits, reported in Table 1. A long sequence of ultra-high-cadence imaging from 2021-02-18 has been averaged together to a single measurement.

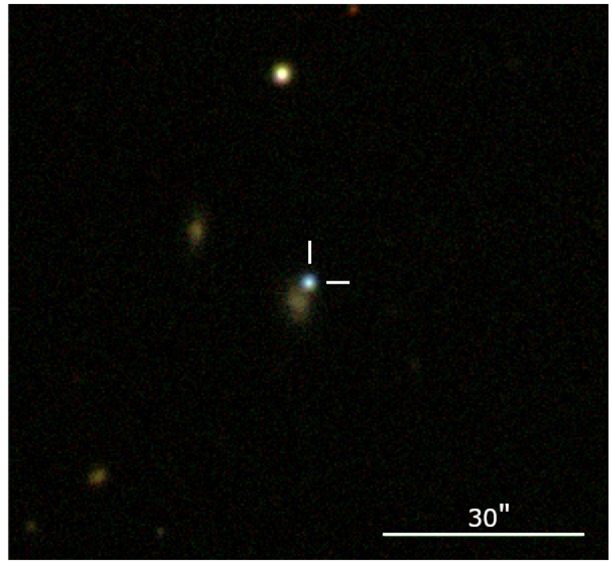

Figure 1. A false-color *gri* image of the field from 2021-02-11 taken with IO:O on the Liverpool Telescope. North is up and East to the left. SN 2021csp is seen as a blue source in an outer spiral arm of its host galaxy, northwest of the nucleus.

We also conducted a more extensive search of the P48 data for pre-explosion outbursts following the procedure described by Strotjohann et al. (2021). No significant detections prior to the explosion date were found, to typical (median) limits of ∼21 mag (−17 absolute magnitude) in 1-day bins or to ∼22 mag (−16 absolute magnitude) in bins up to 90 days in width. These limits rule out only the most luminous pre-explosion outbursts (Strotjohann et al. 2021).

2.2. *Imaging*

2.2.1. *Liverpool Telescope*

We obtained *ugriz* imaging using the Infrared/Optical Imager (IO:O) on the 2m robotic Liverpool Telescope (LT; Steele et al. 2004) starting from the first night following the discovery and continuing until the object faded below detection (55 days later). Data are reduced by the IO:O automatic pipeline and obtained in reduced form from the LT archive. We subtract reference imaging from Pan-STARRS (*griz* bands) or from SDSS (u band) using a custom IDL subtraction pipeline, and perform seeing-matched aperture photometry. A color image of the field is shown in Figure 1.

2.2.2. *Palomar 60-inch Telescope*

We obtained additional *ugri* photometry using the Rainbow Camera of the Spectral Energy Distribution Machine (SEDM; Blagorodnova et al. 2018), on the robotic Palomar 60-inch telescope (P60; Cenko et al.

2006). Image subtraction and photometry was performed using `FPipe` (Fremling et al. 2016).

2.2.3. *Swift Ultraviolet/Optical Telescope*

We observed the field of SN 2021csp with the Ultraviolet/Optical Telescope (UVOT; Roming et al. 2005) on board the Neil Gehrels *Swift* Observatory (Gehrels et al. 2004) beginning 2021-02-12 and continuing until the flux from the transient faded below detectability a month later. An additional set of observations between 2021-03-31 and 2021-04-21 were acquired to constrain the host-galaxy flux. The brightness in the UVOT filters was measured with UVOT-specific tools in the HEAsoft version 6.26.1. Source counts were extracted from the images using a circular aperture of radius $3''$. The background was estimated over a significantly larger area close to the SN position. The count rates were obtained from the images using the *Swift* tool `uvotsource`. They were converted to AB magnitudes using the UVOT photometric zero points in Breeveld et al. (2011) and the UVOT calibration files from September 2020. To remove the host from the transient light curves, we used templates formed from our final observations in April and from archival UVOT observations of the field from 2012. We measured the host contribution using the same source and background apertures, and subtracted this contribution from the transient flux measurements.

2.2.4. *Nordic Optical Telescope*

We obtained four epochs of imaging with Alhambra Faint Object Spectrograph and Camera (ALFOSC) on the 2.56 m Nordic Optical Telescope (NOT). Observations were obtained on 2021-04-03, 2021-04-18, 2021-04-20, 2021-05-07, and 2021-07-01. For the first two epochs, *gri* observations were obtained, and for the last three epochs only deep *r*-band observations were taken. All observations were taken under clear skies and subarcsecond seeing except the data from 2021-04-18 which was affected by thin clouds and relatively poor seeing ($\sim$1.3$''$). Data were reduced with the python package PyNOT[1] (v0.9.7).

For the three sets of observations taken in April, we employ Pan-STARRS templates for subtraction using the same methods used for the LT photometry. By the time of the observation in May, the transient had faded to a very faint level and this method was no longer sufficient: while a secure limiting magnitude of $r > 23.66$ can be obtained from the Pan-STARRS subtraction, this is limited entirely by the depth of the reference (the true 3σ limiting magnitude of this image, measured away from the galaxy, is $r \sim 26.2$.). Instead, we employ the software utility GALFIT (Peng et al. 2002, 2010) to model the disk of the galaxy as a Sérsic profile (convolved with the PSF) and remove it from our images. The model provides only incomplete removal of the inner galaxy light, and the inner spiral pattern and H II regions are visible as residuals in the subtracted image. However, the immediate vicinity around the location of the transient does not show any major residuals (Figure 2), including any evidence of light from the transient. Forced photometry at the transient location gives $r = 25.4 \pm 0.15$, although the flux is probably dominated by light from an unsubtracted H II region just outside the aperture. As a conservative upper limit, we report $r > 24.8$ in our photometry table (corresponding to 5σ above the forced-photometry value in flux units).

The observation from July is not as deep as the one obtained in May and so is not individually constraining. To confirm the accuracy of our GALFIT subtraction, we carried out image subtraction between the May and July observations and obtained an upper limit (difference magnitude) of $r > 25.1$ (3σ). However, since we cannot rule out the possibility that a small amount of flux is present in the July observation, we will generally use the more conservative GALFIT-based approach.

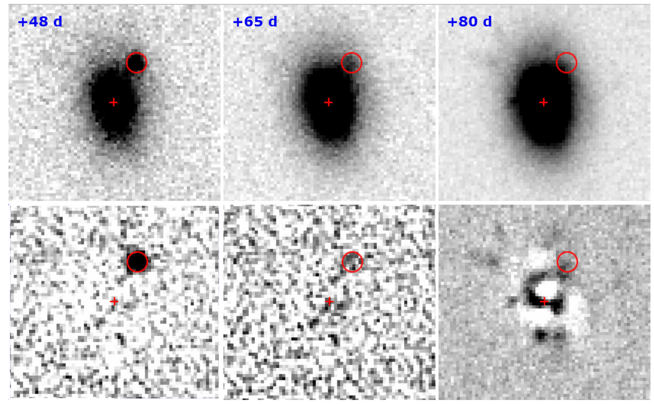

Figure 2. Nordic Optical Telescope imaging of SN 2021csp during the rapid late-phase light curve decline. The top row shows the images without image subtraction, the bottom row shows images after subtraction of the host galaxy. The center of the host galaxy is marked with a cross and the position of the supernova with a circle of $0\farcs7$ radius in all images. Pan-STARRS imaging has been used to subtract the images at +48 and +65 days, although the subtraction at +65 days is limited by the depth of the reference. GALFIT has been used to subtract an axisymmetric model of the host to obtain the image at lower right. No source is detected at the SN location in this image.

2.3. *Spectroscopy*

[1] https://github.com/jkrogager/PyNOT

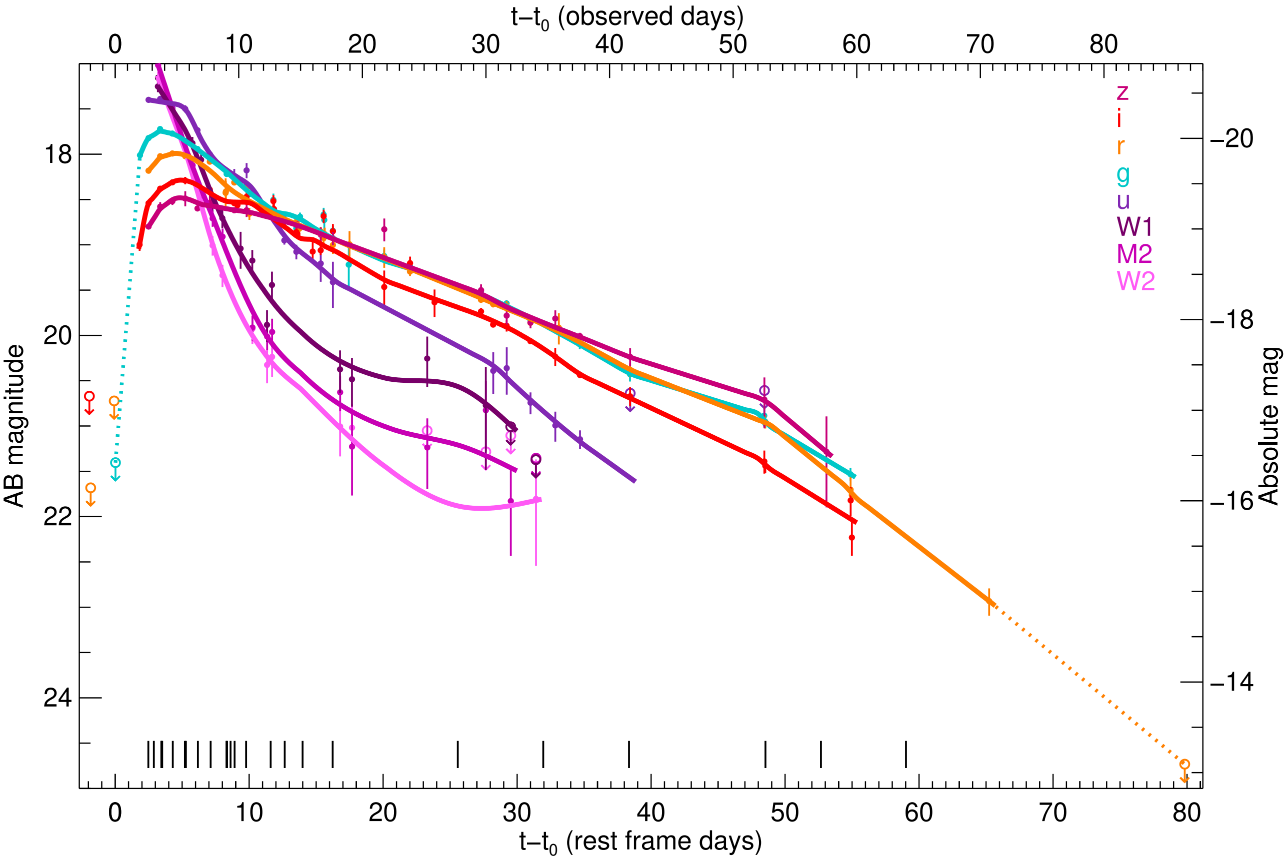

Figure 3. The ultraviolet/optical/near-IR light curves of SN 2021csp. The transient reached a peak absolute magnitude of $M_g \approx -20.1$ (and a bolometric luminosity $L_{\rm bol} > 10^{44}$ erg s^{-1}) within four days of explosion and then rapidly faded, qualifying it as one of the most nearby examples of a fast blue optical transient. Interpolation curves for each filter band are estimated using a combination of local regression and spline fitting. Dotted lines connect the most constraining upper limit with the first detection in the same band, and the last detection with the first subsequent deep upper limit. Bars at the bottom indicate observation times of spectroscopy.

We obtained an extensive series of optical spectroscopy, beginning prior to the peak of the SN and extending until 80 days post-explosion in the rest frame. A log of all spectroscopic observations, 25 epochs in total, is provided in Table 2 and the spectra will be uploaded to WISEREP[2]. Details of the observations are provided below. In addition, we use our g- and r-band light curves to perform an absolute calibration and color-correction on each spectrum. We calculate synthetic magnitudes of each (flux-calibrated, pre-corrected) spectrum in both filter and apply a rescaling (to match the absolute fluxes) followed by a power-law correction (to match the colors). At late times > 50 days we apply only the absolute scaling with no color correction. A time series including many of the spectral observations is displayed in Figure 4.

[2] https://www.wiserep.org

2.3.1. *Liverpool Telescope*

We obtained seven sets of spectroscopy (each 2×600 s) spanning the first two weeks after explosion using the Spectrograph for the Rapid Acquisition of Transients (SPRAT; Piascik et al. 2014). We use the default reduction and extraction provided by the SPRAT pipeline. The first LT spectrum immediately established the redshift and unusual nature of this transient on the basis of the detection of several strong carbon features at a common redshift of $z = 0.084$ (Perley et al. 2021a), motivating the subsequent densely-sampled spectroscopic campaign.

2.3.2. *Gemini-North*

One spectrum was obtained on 2021-02-12 with the Gemini Multi-Object Spectrograph (GMOS; Hook et al. 2004) mounted on the Gemini North 8m telescope at the Gemini Observatory on Mauna Kea, Hawaii. Two 900 s exposures were obtained with the B600 grating.

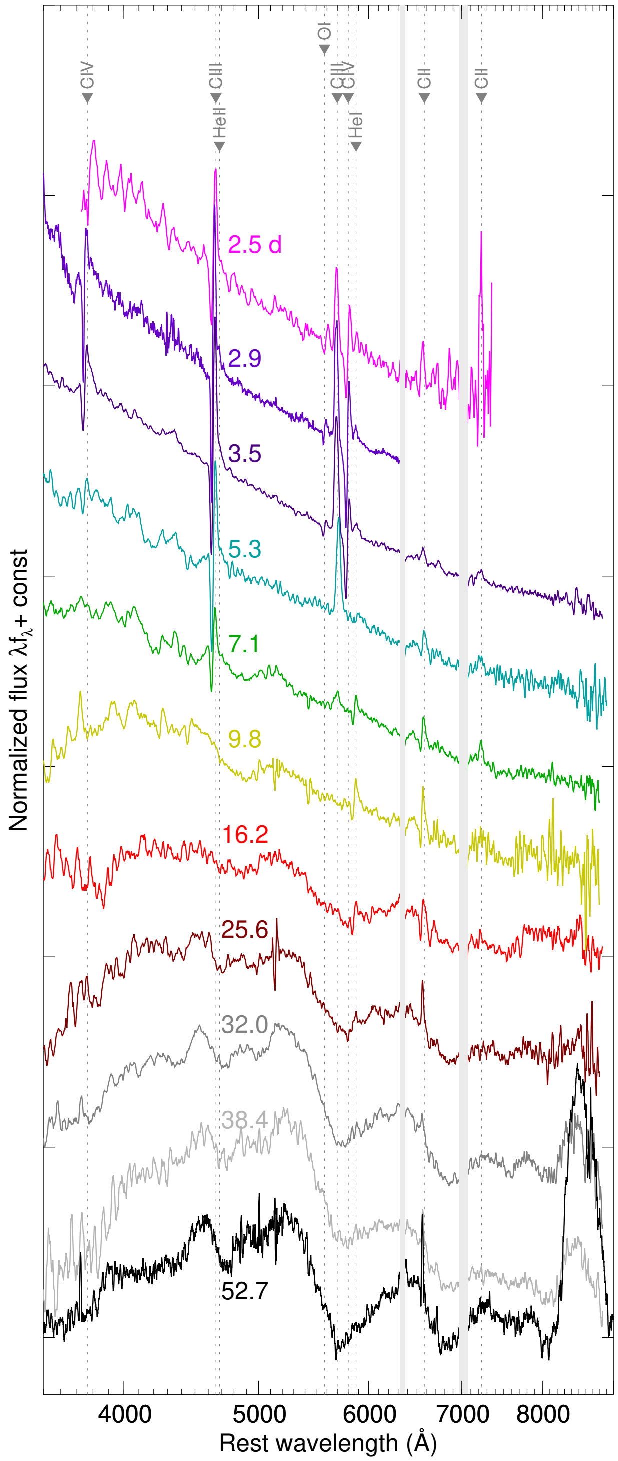

Figure 4. Spectral evolution of SN 2021csp from selected observations (see Table 2 for the full observing log). Early-phase spectra are dominated by narrow P-Cygni features of ionized carbon, which abruptly vanish between 8–12 days post-explosion (rest frame). Broad lines are dominant between 15–53 days. Spectra taken after 53 days show only host-galaxy flux and are not shown here.

The GMOS data were reduced using `Pypeit` (Prochaska et al. 2020).

2.3.3. *Nordic Optical Telescope*

We obtained nine separate epochs of spectroscopy with the ALFOSC on the NOT spanning from 2021-02-13 until 2021-04-03 (Table 2). Observations were taken using Grism #4, providing wavelength coverage over most of the optical spectral range (typically 3700–9600 Å). The slit was aligned with the parallactic angle, except in the last three observations when it also included the host, and an ADC was used. Reduction and calibration were performed using `Pypeit`.

2.3.4. *Very Large Telescope*

Spectropolarimetry of SN 2021csp was conducted with the FOcal Reducer and low dispersion Spectrograph (FORS2) on Unit Telescope 1 (UT1, Antu) of the ESO Very Large Telescope (VLT). The observations were carried out in the Polarimetric Multi-Object Spectroscopy (PMOS) mode on the night of UT 2021-02-13. Two sets of exposures were obtained, and each set includes four 750 s integrations at retarder angles of 0, 22.5, 45, and 67.5 degrees. Grism 300V and a $1\farcs0$ wide slit was used, resulting in spectral resolving power of $R \sim 440$ at a central wavelength of 5849 Å. Filter GG435, which has a cut-on at $\sim$4400 Å was in place to prevent contamination from the second-order beam. This configuration provides a wavelength range of $\sim$4400−9200 Å in the observer frame. The total spectrum was flux-calibrated based on the observation of a spectrophotometric standard star using the same instrumental setup but only at the half-wave plate angle 0 degrees.

The data were bias subtracted and flat-field corrected. For each individual exposure, the ordinary (o) and extraordinary (e) beams were extracted and wavelength-calibrated separately following standard procedures within IRAF (Tody 1986). After removing the instrumental polarization of FORS2 (Cikota et al. 2017), we derived the Stokes parameters, the bias-corrected polarization, and the associated errors using our own routines, following the procedures in Patat & Romaniello (2006); Maund et al. (2007); Simmons & Stewart (1985); Wang et al. (1997). A detailed description of the reduction of FORS spectropolarimetry can be found in Yang et al. (2020, their Appendix A).

The Stokes parameters computed for each set of the four exposures are consistent with each other. We further combined the two beams for o-ray and e-ray at each retarder angle and derived the Stokes parameters. The intensity-normalized Stokes parameters (I; Q; U) are binned in 75 Å wide bins ($\sim$22 pixels) to further increase

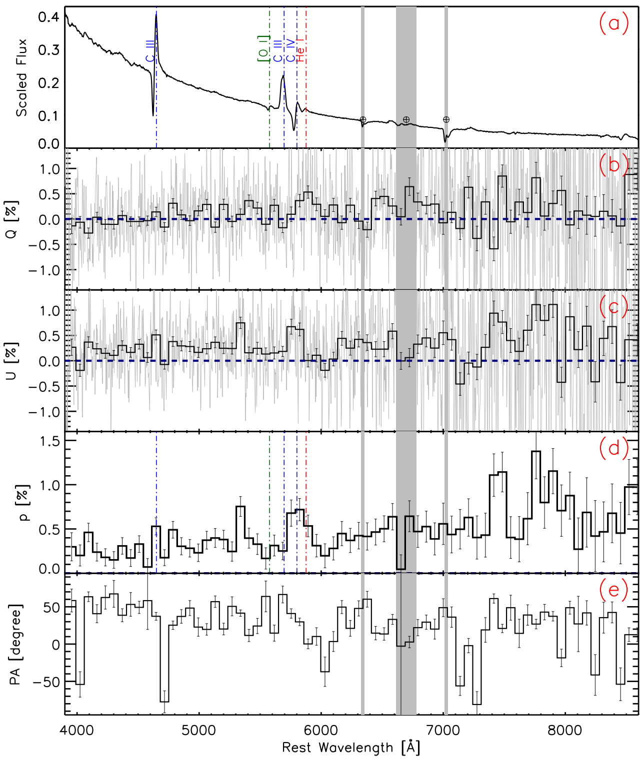

Figure 5. Spectropolarimetry of SN 2021csp at ∼3.5 days (rest-frame). The five panels (from top to bottom) show (a) the scaled total flux spectrum with C III, C IV, [O I], and He I lines labeled at zero velocity relative to the SN; (b) the normalized Stokes Q; (c) the normalized Stokes U; (d) the polarization spectrum (p); and (e) the polarization position angle (PA). Vertical gray-shaded regions indicate the major tellurics. The data have been rebinned to 75 Å for clarity.

the signal-to-noise ratio (S/N). The result is presented in Figure 5.

2.3.5. *Lick 3m Telescope*

A single optical spectrum of SN 2021csp was obtained with the Kast Double Spectrograph (Miller & Stone 1993) mounted on the 3 m Shane telescope at Lick Observatory. The spectrum was taken at or near the parallactic angle (Filippenko 1982) to minimize slit losses caused by atmospheric dispersion. Data were reduced following standard techniques for CCD processing and spectrum extraction (Silverman et al. 2012) utilizing IRAF routines and custom Python and IDL codes[3]. Low-order polynomial fits to arc-lamp spectra were used to calibrate the wavelength scale, and small adjustments derived from night-sky lines in the target frames were applied. Observations of appropriate spectrophotometric standard stars were used to flux calibrate the spectra.

2.3.6. *Hubble Space Telescope*

We obtained two sets of observations of SN 2021csp with the Hubble Space Telescope (HST), using both the Cosmic Origins Spectrograph (COS) and the Space Telescope Imaging Spectrograph (STIS)[4]. The COS observations employed the G140L grating and the STIS observations used the G230L grating. The first set of observations was taken at 8.31 and 8.61 rest-days after our assumed explosion time (for STIS and COS, respectively); the second set were taken at 11.61 days (STIS) and 13.99 days (COS).

We use the pipeline reductions from the HST archive. The first STIS spectrum shows a S/N about a factor of 10 lower than expected, likely due to a guiding problem. This problem is not seen in the second STIS exposure or with COS. The UV spectra are shown alongside optical spectra obtained at similar times in Figure 6.

2.3.7. *Palomar 200-inch Telescope*

One spectrum of SN 2021csp was acquired with the Double Beam Spectrograph (DBSP; Oke & Gunn 1982) on the 5m Hale telescope at Palomar Observatory (P200). Observations were taken on 2021-04-09, using the 600/4000 grating on the blue side and the 316/7150 grating on the red side. Data were reduced using the DBSP-DRP fully-automated pipeline (dbs 2021).

2.3.8. *Keck Observatory*

Spectroscopy of SN 2021csp was acquired on four separate occasions with the Low Resolution Imaging Spectrometer (LRIS, Oke et al. 1995) on the Keck I telescope. The first observation was acquired on 2021-04-07 using the B600/4000 blue-side grism and the R400/8500 red-side grating; the remaining three observations (on 2021-04-14, 2021-05-10, and 2021-05-16) were all acquired with the B400/3400 grism and the R400/8500 grating. Weather conditions were generally good except for the observation on 2021-05-10, which was taken under clear skies but very poor seeing (2–3″). Because of the different readout times the exposure durations on LRIS vary between red and blue sides; in Table 2 we represent the individual exposures with average exposure time (over all exposures on both sides) for simplicity.

All spectra were reduced with LPipe (Perley 2019). The two LRIS spectra in May do not show any discernable trace from the SN in the 2D frames. For the spectrum taken on 2021-05-16 we determine the position of the SN along the slit via its offset from the host nucleus (this slit was oriented across the nucleus at a PA

[3] https://github.com/ishivvers/TheKastShiv

[4] program ID GO#16212 (PI: Perley)

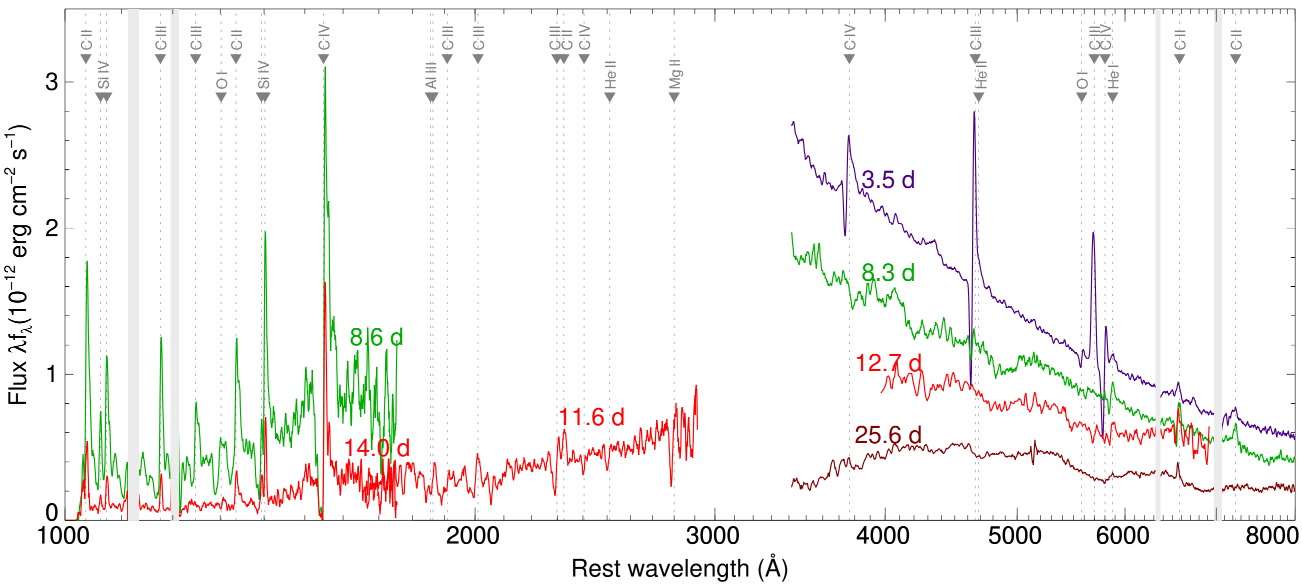

Figure 6. Combined UV-optical spectral series showing the relative strengths of the narrow emission features at various approximately co-eval epochs (all times are rest-frame days from the assumed explosion time). Identified transitions are marked with dotted lines, and regions of strong telluric absorption or geocoronal contamination are marked with gray bands.

of −50 degrees) and extract the flux at this location. We also separately extract the flux of the entire host galaxy along the slit for spectroscopic analysis of the host. (For the observation on 2021-05-10, the seeing is too poor to attempt separate site and host extractions and we simply extract the host, but we do not use this spectrum in our subsequent analysis.)

2.4. *Multiwavelength*

2.4.1. *Swift/XRT*

We observed the field with *Swift*'s onboard X-ray Telescope (XRT, Burrows et al. 2005) in photon-counting mode, simultaneous with each set of UVOT observations (2.2.3). There is no detection of the SN in any of these observations. Using the online tool[5] provided by the UK Swift team (Evans et al. 2007, 2009), we infer a median upper limit of ≈ 0.006 ct s^{-1} per epoch at 3σ confidence. Stacking all data lowers the upper limit to 0.0008 ct s^{-1}. Assuming a Galactic neutral hydrogen column density of $n(H) = 2.4 \times 10^{20}$ cm^{-2} (HI4PI Collaboration et al. 2016) and a power-law spectrum with photon index of 2, the count rates correspond to an unabsorbed flux limit of 2.2×10^{-13} and 3.1×10^{-14} erg cm^{-2} s^{-1} in the bandpass 0.3–10 keV, respectively. At the distance of SN 2021csp this corresponds to luminosity $L < 3.8\times10^{42}$ erg s^{-1} and $L < 5.4\times10^{41}$ erg s^{-1} between 0.3–10 keV, respectively.

2.4.2. *Very Large Array*

We obtained three epochs of Very Large Array (VLA) observations of SN 2021csp: one each on 2021-02-17, 2021-03-10, and 2021-07-10[6]. In each observation the phase calibrator was J1430+1043 and the flux calibrator was 3C286. Data were calibrated using the automated pipeline available in the Common Astronomy Software Applications (CASA; McMullin et al. 2007) and additional flagging was performed manually. Data were imaged using the `clean` algorithm (Högbom 1974) with a cell size 1/10 of the synthesized beamwidth, and a field size of the smallest magic number (10×2^n) larger than the number of cells needed to cover the primary beam. In the first observation the VLA was in A configuration and we found a non-detection with an RMS of 5 μJy. During the second observation the VLA was changing configuration from A to D. We found another non-detection with an RMS of 5 μJy. These measurements imply limits (3σ) of 2.6×10^{-27} erg s^{-1} cm^{-2} Hz^{-1} at 7 and at 26 days post-explosion (rest-frame). **Latest observation will be added when NRAO archive comes back online.**

2.4.3. *High Energy Counterpart Search*

We searched the Fermi GBM Burst Catalog (Narayana Bhat et al. 2016), the Fermi-GBM Subthreshold Trigger list, the Swift GRB Archive, the IPN master list, and the Gamma-Ray Coordinates Network archives for a GRB between the last ZTF non-detection and the first ZTF detection. The closest event was one Fermi

[5] http://www.swift.ac.uk/user_objects/

[6] Program IDs 20B-205 and 21A-308; PI Ho

burst (GRB210210B) 16 degrees away, but the association is unlikely given the size of the localization region. There was one IceCube event in the relevant time interval, but due to the 10-degree separation we consider the association unlikely.

2.5. *Host Galaxy Photometry*

We retrieved science-ready coadded images from the Sloan Digital Sky Survey data release 9 (Ahn et al. 2012), UKIRT Infrared Deep Sky Survey DR11Plus (Lawrence et al. 2007), and preprocessed *WISE* (Wright et al. 2010) images from the unWISE archive (Lang 2014). The unWISE images are based on the public *WISE* data and include images from the ongoing NEOWISE-Reactivation mission R3 (Mainzer et al. 2014; Meisner et al. 2017). In addition to this, we use the UVOT observations that were obtained either before the explosion of SN 2021csp or after the SN faded from visibility. The brightness in the UVOT filters was measured with UVOT-specific tools in the HEAsoft[7]. Source counts were extracted from the images using a region of 10″. The background was estimated using a circular region with a radius of 33″ close to the SN position. Count rates were obtained from the images using `uvotsource`. They were converted to AB magnitudes using the UVOT calibration file from September 2020.

We measured the brightness of the host using LAMBDAR (Wright et al. 2016), `uvotsource`, and the methods described in Schulze et al. (2020). Table 3 provides the measurements in the different bands.

3. ANALYSIS

3.1. *Light Curve*

3.1.1. *Explosion Time*

SN 2021csp was identified prior to peak and recent upper limits are available, permitting a reasonably tight constraint on the time of first light (defined here as the moment when optical photons in excess of the progenitor luminosity are first able to escape and travel freely towards the observer). We will refer to this as the "explosion time" for simplicity, although we emphasize that the data can not actually separately distinguish the time of core-collapse or shock breakout.

The most recent ZTF/P48 upper limit prior to the discovery is from an observation at MJD 59254.52578 ($g > 21.50$ mag, 2.5σ), which is 1.94 days prior to the first detection in i band and 1.97 days prior to the first detection in the g band. Assuming an early flux evolution following $F \propto t^2$, the earliest explosion time consistent with the early g-band limit is $\mathrm{MJD_{exp}} > 59254.0$. This limit is likely to be conservative, since the flux was already turning over from a t^2-like early behavior at the time of the initial detections.

No upper limit can be formally placed on the time of explosion other than the time of the first detection itself since the rising phase is too short and poorly-sampled to be modeled effectively. The (very conservative) upper limit is thus $\mathrm{MJD_{exp}} < 59256.47$. Given that the source was already quite bright at this time, our general expectation (supported by the blackbody modeling; §3.1.3) is that the explosion time is probably closer to the beginning of the constrained window.

Throughout the remainder of the paper we will express observation times in the rest frame relative to 59254.5 MJD, the approximate time of the last upper limit and a reasonable guess of the time of explosion. Expressed in this system, our constraint on the actual time of explosion is $-0.46\,\mathrm{d} < t_{\mathrm{exp}} < 1.82\,\mathrm{d}$.

3.1.2. *Characteristic Timescale*

To better quantify the rapid evolution of SN 2021csp and compare it to other optical transients, we perform a basic measurement of the characteristic evolutionary timescales.

The rise time (t_{rise}, defined as the rest-frame time from explosion to peak) depends on the band, with redder filters showing later peaks (and therefore longer rise times). In the g band where the early light curve is best sampled, the rise time is 1.8–4.0 rest-frame days, with the large uncertainty primarily originating from the uncertainty on the explosion time itself (although following the arguments in § 3.1.1, times towards the upper end of this range are likely more plausible). The rise time is $\sim$1 day longer in r and $\sim$ 1.5 days longer in i and z.

For comparison to the light curves of other SNe, a standard metric is the half-max time $t_{1/2}$, the amount of time (rest-frame) which the transient spends at a flux level more than half of its maximum in some wavelength band. This can be decomposed into separate half-rise ($t_{1/2,\mathrm{rise}}$) and half-fade ($t_{1/2,\mathrm{fade}}$) times, the intervals over which the transient takes to rise from half-maximum to maximum and the time the transient takes to fade from maximum to half-maximum (respectively). The smoothed interpolation of our g-band light curve gives a half-rise time of $t_{1/2,\mathrm{rise}} = 2.5 \pm 0.5$ days and a half-fade time of $t_{1/2,\mathrm{fade}} = 8.3 \pm 1$ days, for a total time above half-max of $t_{1/2} = 10.8 \pm 1.2$ days. (The r-band timescale is somewhat slower, with $t_{1/2} \sim 15$ days).

A comparison between the characteristic timescales and luminosities of SN 2021csp and similarly-measured estimates for a variety of other "fast" transients is shown

[7] https://heasarc.gsfc.nasa.gov/docs/software/heasoft/

in Figure 7. SN 2021csp is much more extreme than SN 2019hgp and fits in well with the population of spectroscopically-unclassified fast and luminous optical transients from the works of Drout et al. (2014) and Pursiainen et al. (2018) (gray circles).

More recently, Ho et al. (2021) compiled a large catalog of rapidly-evolving events with spectroscopic classifications from the ZTF partnership surveys (1 day cadence or faster); Perley et al. (2020) produced a spectroscopically-complete catalog of events from the ZTF public Bright Transient Survey (3-day cadence). The samples from these two surveys are added to Figure 7 for comparison. Consistent with its spectroscopic properties, SN 2021csp is sited in the same region of parameter space occupied by interaction-dominated transients (primarily Type Ibn and fast Type IIn supernovae; see Ho et al. 2021). However, it is among the most luminous examples of this group and also one of the fastest-rising, bringing it somewhat closer to the "Cow-like" radio-loud population in the top left of Figures 7a-b than to typical SNe Ibn.

3.1.3. *Blackbody modeling*

To obtain common-epoch spectral energy distributions (SEDs), we define a set of standardized epochs (chosen to be close in time to actual multi-band measurements) and use a combination of local regression smoothing and spline fitting to obtain interpolated light curve measurements for all available filters at each point. After correcting for Galactic extinction, we then fit a Planck function to each set of fluxes to determine the effective temperature, photospheric radius, and luminosity. The host extinction $E_{B-V,\rm host}$ is initially assumed to be zero (based on the face-on geometry of the host, the outlying location of the event, and the lack of narrow ISM absorption lines in the spectra), but we later repeat the procedure under different assumptions about the host reddening.

The results of our blackbody fits are shown in Figure 8, where they are compared to a variety of other fast and/or luminous transients measured using similar approaches. The fast rise to peak implies an initial velocity that is very high (~ 30000 km s^{-1}), akin to what is seen in SNe Ic-BL. (The individual SED fits are given in the Appendix.)

The subsequent evolution is generally normal, in the sense that the luminosity and temperature decline while the radius increases, reaches a maximum, and then recedes into the cooling ejecta. The final two points should be treated with caution, since at this point the spectrum has heavily diverged from a simple blackbody (Figure 4) and the UV emission is weak or absent.

We examined whether the possibility of host extinction would alter any of the conclusions above. For a Milky Way-like reddening law (Fitzpatrick 1999), the maximum potential extinction permitted by our SED models is $E_{B-V,\rm host} = 0.15$ mag (higher extinction values lead to poor fits at early times because the corrected fluxes become too blue for a blackbody model.) The inferred luminosity and temperature both increase significantly at early times in this scenario, but the radius measurements are affected by only 10–20% (see dotted lines in Figure 8). For the remainder of the discussion we will continue to assume $E_{B-V,\rm host} = 0$.

3.2. *Spectral analysis*

The spectroscopic sequence shown in Figure 4 shows two distinct regimes. Between 2–10 days, the spectra are characterized by a hot blue continuum superimposed with very strong narrow features ("narrow phase"). After 16 days, the narrow lines have disappeared completely and series of broad features with velocities characteristic of SN ejecta emerge instead ("broad phase"). The spectrum in between these two periods (i.e., 10–16 days) exhibits a brief transitional state in which most of the narrow optical features have vanished *but* C II remains and the UV P-Cygni features also remain very strong, and whereas broad features are becoming evident in the spectrum they are still weak and indistinct. We summarize the key features of the two spectral regimes below.

3.2.1. *Narrow-phase spectra*

All identified strong lines spanning the UV to 8000 Å are shown in Figure 6, with zoom-ins on various strong features presented in Figure 9 and Figure 10. Almost all of the identifiable lines are associated with oxygen, carbon, silicon, or magnesium. He II may be present in a blend with the C III λ4656 feature, although because of the high velocities this cannot be conclusively established. However, He I λ5876 is clearly seen. Some of the later spectra show a P-Cygni feature close to the position of Hα λ6563, although more likely this feature originates from a combination of C II λ6580 (which persists longer than the other lines) and host-galaxy narrow emission. Most line profiles have a P-Cygni shape, with blueshifted absorption and emission that may be either net blueshifted or net redshifted depending on the line and phase. The far-UV Si lines are seen only in emission, as is C III λ5696.

Despite being qualitatively characterized as narrow lines, the velocities inferred from these features are quite high. The deepest point of absorption in the strong lines from the early, high-S/N optical spectra is at -2200 km s^{-1}, with a maximum blueshift (blue edge) of -3000 km

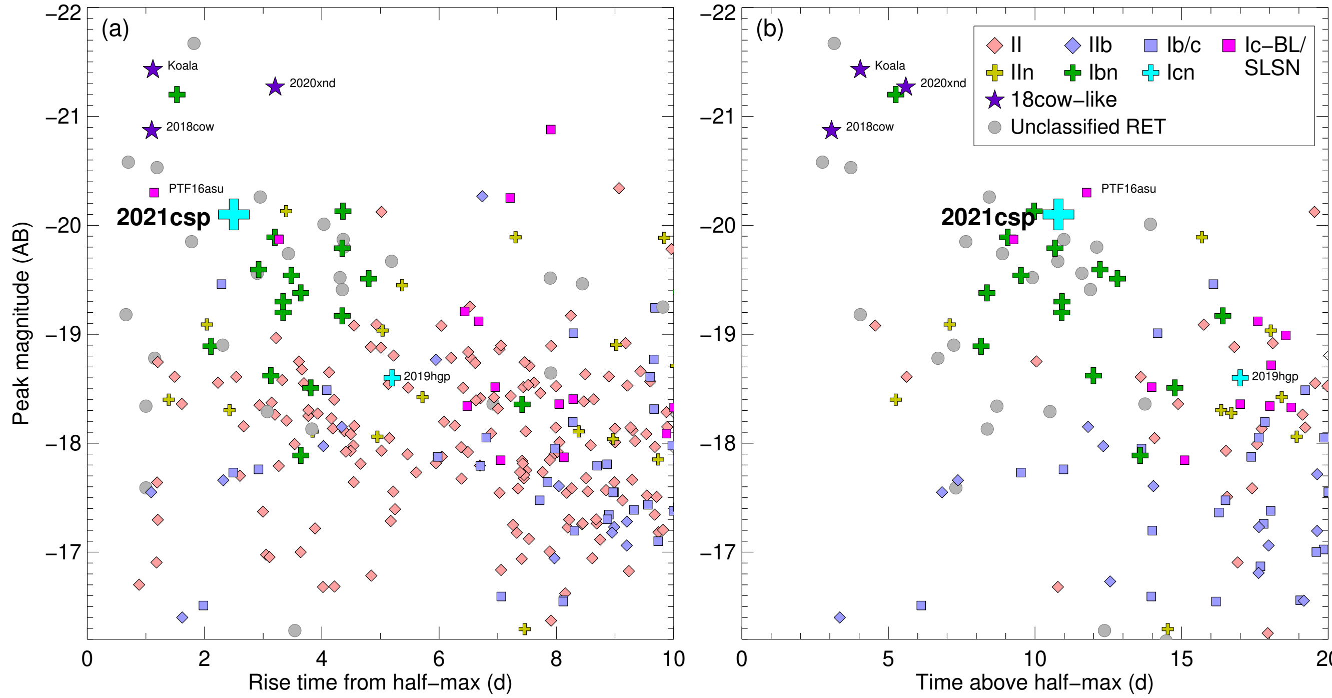

Figure 7. Characteristic timescales for SN 2021csp compared to the known population of core-collapse transients from the ZTF Bright Transient Survey (Perley et al. 2020) and to fast transients ($t_{1/2} < 12$ d) from the literature (Drout et al. 2014; Pursiainen et al. 2018; Ho et al. 2019a, 2021). Figure (a) at left shows the rise time from half-maximum to maximum ($t_{1/2,\mathrm{rise}}$) on the x-axis; figure (b) at right shows the total time above half-maximum ($t_{1/2}$) on the x-axis. SN 2021csp groups most naturally with SN Ibn explosions, although it shares some features with the AT 2018cow-like population seen in the top left of both panels.

s^{-1}. The inferred velocities in the UV (where the transitions are much stronger) are even higher; the C IV λ1548 line shows almost-total absorption out to -2000 km s^{-1} but weaker absorption out to a maximum blueshift of approximately -4500 km s^{-1}.

A comparison between the peak-light spectra of SN 2021csp, the prototype Type Icn SN 2019hgp, two SNe Ibn (SN 2019uo and SN 2010al) is displayed in Figure 11. The spectrum of SN 2019uo is the classification spectrum from TNS (Fremling et al. 2019); the spectrum of SN 2010al is taken from Pastorello et al. (2015a). The spectrum of SN 2021csp strongly resembles that of SN 2019hgp, although it lacks some of the transitions seen in that SN (e.g. O III). The line widths in SN 2021hgp are somewhat broader. The features in the Type Ibn SNe (mainly He I) are much weaker, although the line profiles are qualitatively similar.

A comparison versus two Type Ibn SNe in the ultraviolet (SN 2020nxt and SN 2010al; Fox et al. in prep, Kirshner et al. 2010) is provided in Figure 12. Some common transitions are apparent in this regime, most notably the resonance lines of Si IV λ1402 and C IV λ1548, which have similar strengths and profiles. The remaining features are quite different: SN 2021csp shows a number of carbon features absent in SNe Ibn, while the very strong doublet N V $\lambda\lambda$1238,1242 is seen in both Type Ibn SNe but absent entirely in the Type Icn SN 2021csp. Also, while the characteristic velocities are similar, the high-velocity component (4000 km s^{-1}) in absorption and emission seen in SN 2021csp is not clearly visible in either of the SNe Ibn—although the issue is somewhat confused by contamination with other features and the different phases of the observations.

3.2.2. *Broad-phase spectra*

The broad lines are somewhat indistinct between 10–15 days, but by 16 days the characteristic late-time spectrum has clearly emerged. The flux is strongest in the blue, with maxima at 4600 Å, ∼5300 Å, and ∼6400 Å. The relative strength of these features increases gradually with time but neither their shapes nor central wavelengths change much, with the notable exception of the Ca II near-infrared triplet at ∼8540 Å: not apparent at all prior to ∼30 days, it rapidly rises to become the dominant emission feature in our final spectrum at 53 days. The maximum velocity (at zero intensity) on the blueshifted side is ~ -10000 km s^{-1}, characteristic of nebular-phase stripped-envelope SNe.

The identity of the remaining features is less clear. The general shape of the continuum strongly resembles

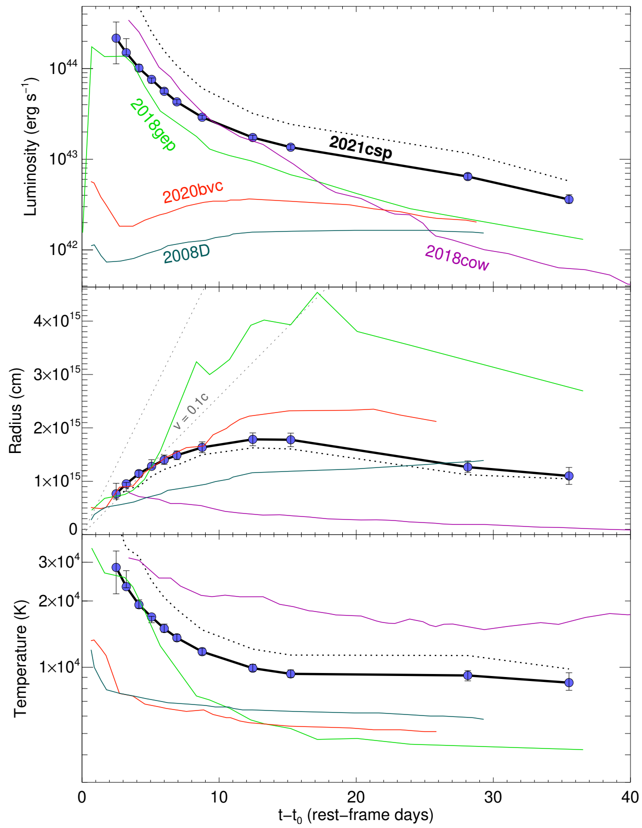

Figure 8. Evolution of photospheric parameters estimated from blackbody fits to the UV-optical SED of SN 2021csp during the first month. The solid black curves show results assuming no host extinction; the dotted curves assume $E_{B-V,\mathrm{host}} = 0.15$ mag. Various comparison objects with fast early evolution from the literature are shown for comparison: SN 2020bvc, a "normal" SN Ic-BL discovered early (Ho et al. 2020b), SN 2018gep (a strongly interacting SN Ic-BL; Ho et al. 2019a), and AT 2018cow (an extreme FBOT which did not develop any late-time supernova; Perley et al. 2019). The radii of all of these explosions are similar at ∼5 days post-explosion, indicating similar ejecta velocities ($v \sim 0.1c$). Different evolution sets in at later phases. (Note: the late rapid downturn is not shown here due to the lack of UV photometry to constrain the temperature after 35 days.)

those of Type Ibn SNe at similar phases, although the narrow He I lines characteristic of SNe Ibn at these phases are absent. In particular, the shape of the continuum in the blue strongly resembles the blue pseudo-continuua seen in Type Ibn SNe, which has been attributed to a forest of blended Fe II lines provided by fluorescence in the inner wind or post-shock gas (Foley et al. 2007; Chugai 2009; Smith et al. 2009; Pastorello et al. 2015b). A comparison between SN 2021csp, SN 2019hgp, and two late-phase SNe Ibn (2006jc from Pastorello et al. 2007 and SN2020eyj from Kool et al., in prep) is shown in Figure 14.

3.3. *Polarimetry*

An upper limit on the interstellar polarization (ISP) induced by dichroic extinction of Milky Way-like dust grains is given by $p_{\rm ISP} < 9 \times E_{B-V}$ (Serkowski et al. 1975). Therefore, we set an upper limit on the ISP from the Galactic component as 0.24%. We assume a host $A_V = 0$ (§3.1.3). We evaluated a continuum polarization level of ∼0.3% by computing the error-weighted Stokes parameters in the optical range after excluding the prominent spectral features and telluric ranges. Therefore, without a careful determination of the ISP from the SN host, we suggest that the continuum polarization of the SN is less than ∼0.5%.

There is no strong polarization signal associated with any of the narrow line features, although the wavelength bins in the vicinity of flash-ionized narrow P-Cygni features of ionized C III and C IV (labeled in Figure 5) do show a polarization excess of about 0.4% above the continuum level at approximately 5σ significance, which may be an indicator of some (limited) asymmetry in the explosion and/or CSM.

Assuming a limiting polarization of 0.5%, the axis ratio of the photosphere can be limited to $\lesssim$1.3 assuming an ellipsoidal surface with a Thomson optical depth of 5 and a radial CSM density profile of $n(r) \propto r^{-n}$, with an index n is in the range from 3–5 (Höflich 1991).

3.4. *Radio Analysis*

The radio limits do not rule out a light curve similar to that seen in ordinary SNe, but the second measurement is significantly fainter than AT 2018cow or AT 2020xnd at a comparable epoch (Ho et al. 2021). A comparison between the upper limits and some previous SN light curves is shown in Figure 16.

3.5. *Host Galaxy*

We modelled the spectral energy distribution with the software package `prospector` (Leja et al. 2017) using the same procedures as in Schulze et al. (2020). We assumed a Chabrier initial mass function (Chabrier 2003), approximated the star formation history (SFH) by a linearly increasing SFH at early times followed by an exponential decline at late times (functional form $t \times \exp\left(-t/\tau\right)$), and a Calzetti et al. (2000) attenuation law.

Figure 17 shows the observed SED and its best fit. The SED is adequately described by a galaxy template with a mass of $\log(\mathrm{M/M_\odot}) = 9.67^{+0.13}_{-0.23}$ and a star-formation rate of $0.69^{+0.53}_{-0.16}\ M_\odot\,\mathrm{yr}^{-1}$.

Emission line fluxes were extracted from the late-time Keck spectroscopy (using the observation from 2021-05-16, which covered the host nucleus and was taken af-

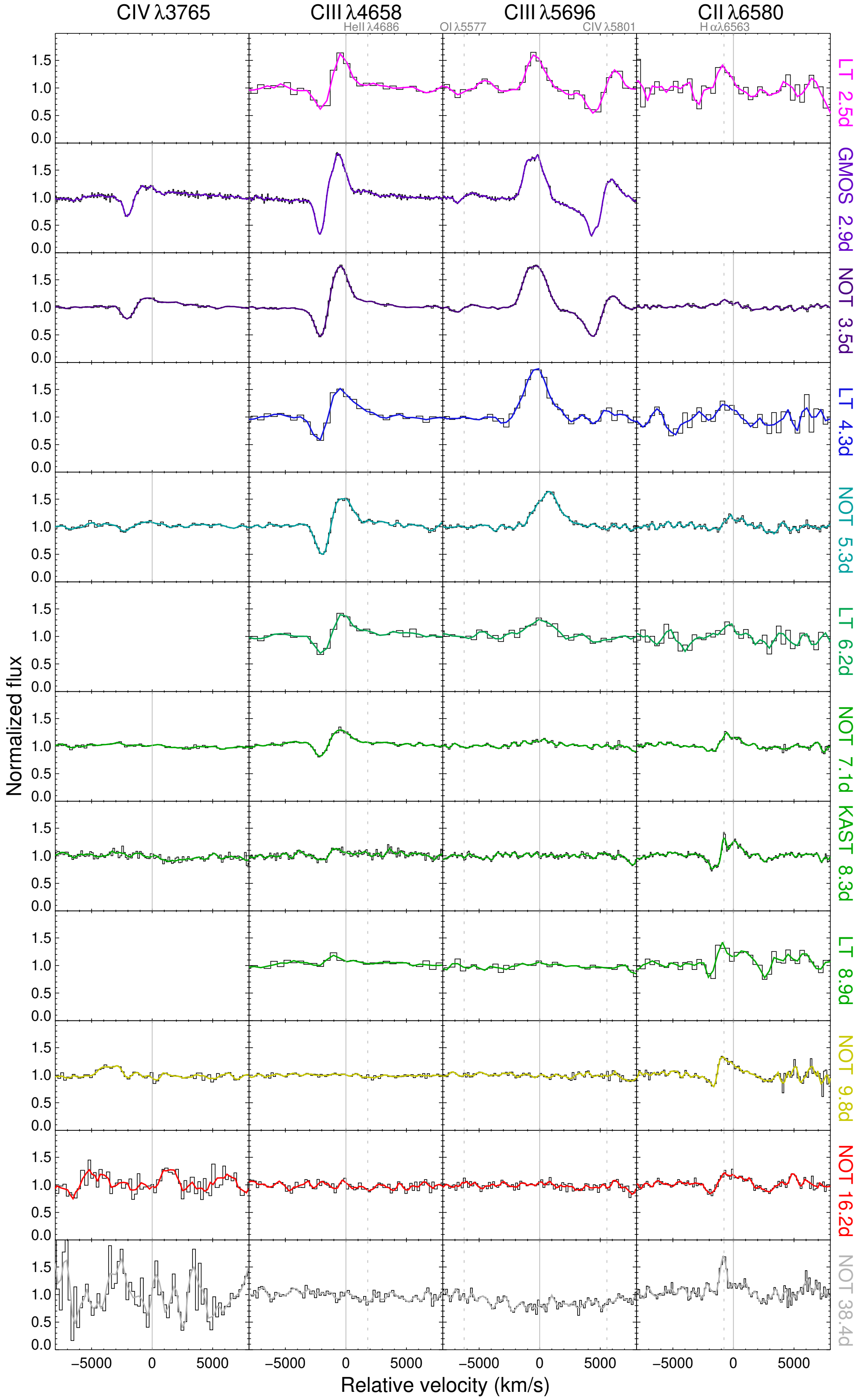

Figure 9. Evolution of selected narrow-line features in the optical range. Original spectra are plotted in black; a smoothing kernel has been applied to the colored curves. Line centers are indicated as a solid line with other nearby (contaminating) transitions indicated as dotted lines. The C IV $\lambda3765$ and $\lambda5801$ features disappear from the optical spectra at approximately 5 days; the C III $\lambda4658$ and $\lambda5696$ features follow at approximately 9 days. Weak C II $\lambda6580$ persists until later times, although becomes contaminated by host-galaxy Hα emission and is difficult to recognize after 16 days.

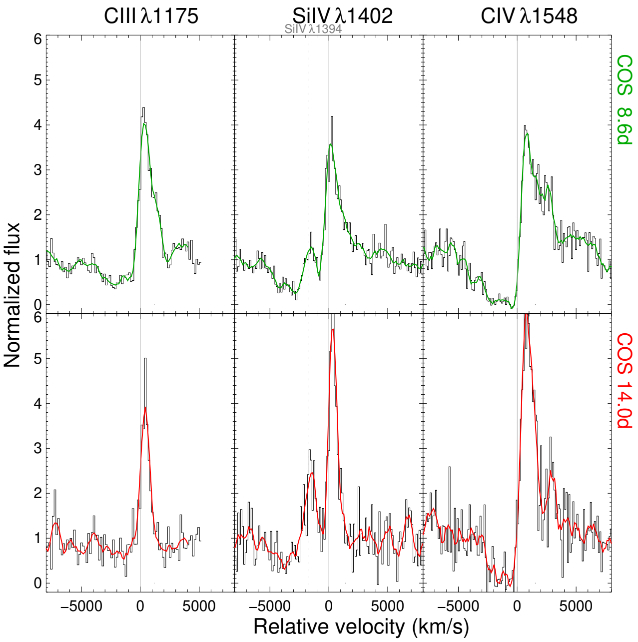

Figure 10. Evolution of narrow-line features (C III λ1175, Si IV λ1402, and C IV λ1548) in the far-ultraviolet range between the two HST epochs. The emission line features remain strong in this wavelength range even after lines of the same species in the optical have disappeared and even after the UV continuum becomes faint.

ter the transient had faded; we use a custom extraction covering the entire host). We measure the following line fluxes for Hα, Hβ, [O III] λ5007, [O III] λ4960, and [N II] λ6585 of 42.2 ± 0.4, 10.8 ± 0.7, 14.1 ± 0.8, 4.3 ± 0.6 and 11.0 ± 0.4, respectively (units of $\times 10^{-16}$ erg cm^{-2} s^{-1}; no extinction correction has been applied). We estimate the metallicity at the galaxy centre using the O3N2 indicator with the calibration reported in Marino et al. (2013). The oxygen abundance of $12 + \log(\mathrm{O/H}) = 8.35 \pm 0.01$ translates to a low metallicity of $0.46 \pm 0.01\ Z_{\odot}$ (assuming a solar oxygen abundance of 8.69; Asplund et al. 2009).

3.6. *Summary of Observational Properties*

The key observational features of the Type Icn SN 2021csp are summarized below:

- SN 2021csp exhibits three distinct phases. At early times ($<$ 10 days), the temperature is very high but rapidly cooling, and the spectra are dominated by strong, narrow P-Cygni features of C and O. At 20–60 days, the spectra are dominated by broad features and there is comparatively little color evolution; the light curve declines gradually. After 60 days, the light curve fades very rapidly and the transient disappears (absolute magnitude $M_r > -13$) by 80 days.
- The spectra are dominated by carbon and oxygen, with silicon also evident in the UV and an iron pseudo-continuum visible in the broad-component phase in the blue. Compared to Type Ibn supernovae, helium is weak and nitrogen is absent. The strength of the narrow lines is greater than in any known SN Ibn close to peak, but narrow lines are lacking entirely at late times.
- Several characteristic velocities are evident. The "narrow" features show maximum absorption at 2000 km s^{-1} with maximum velocity 4500 km s^{-1}, indicative of the velocity of the CSM. The early photospheric modeling indicates the existence of a high-velocity ejecta component with 30000 km s^{-1}. Late-phase optical spectra suggest a characteristic ejecta velocity of 10000 km s^{-1}.
- The very fast rise (3 days) and high peak luminosity ($M_g \sim -20$) are consistent with common definitions for a "FBOTs", but these values are not unusual for Type Ibn SNe, many of which have also been shown to be "FBOTs". (Ho et al. 2021).
- There is no detection of a radio or X-ray counterpart. The limits rule out an 18cow-like event or GRB, but not most classes of normal supernovae.
- The transient occurred in the outer regions of a moderately low-mass, star-forming spiral galaxy.

In the following section we interpret these observations in the context of the progenitor star, its CSM, and the nature of the explosion itself.

4. DISCUSSION

4.1. *A highly chemically-evolved progenitor*

The spectroscopic observations reveal a progenitor star that has lost all of its hydrogen, and which is also depleted in helium and nitrogen. These properties describe both the narrow (CSM) features and the broad (ejecta) features, and it is clear that the supernova represents the explosion of a heavily stripped star into a dense nebula of material recently expelled from its surface.

An important question is whether the weak helium features indicate a qualitatively distinct composition from Type Ibn SNe or merely a difference in ionization. Helium can be a notoriously difficult element to interpret in SN spectra, since non-LTE effects are required for He features to be observable (Li et al. 2012; Dessart et al. 2012). The almost-complete lack of nitrogen (alongside that of helium) provides a powerful argument to support the case that the composition is genuinely distinct from

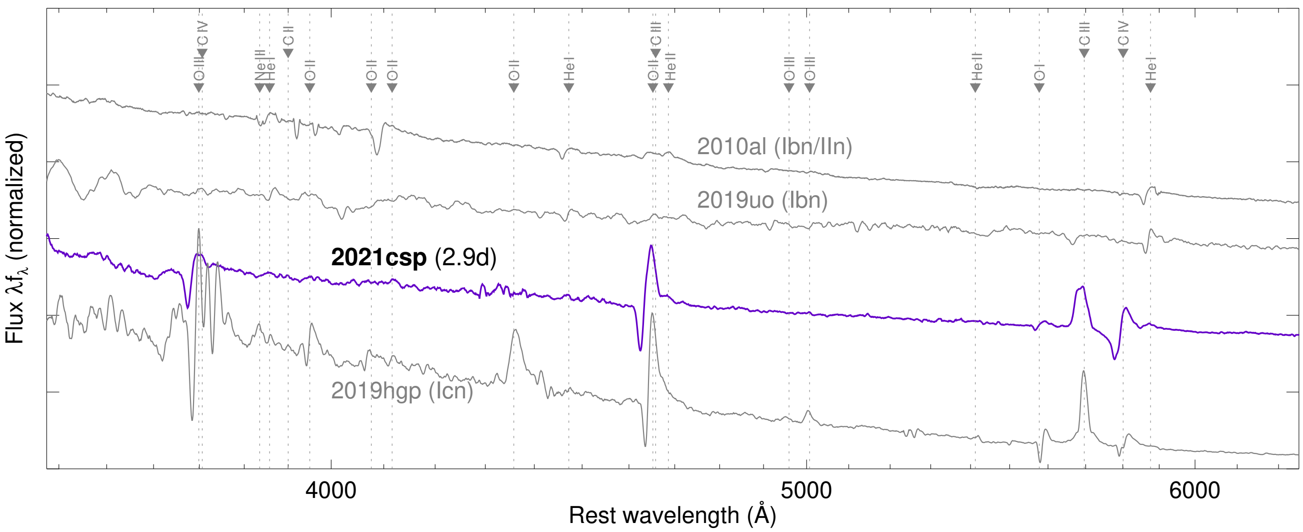

Figure 11. Peak-light spectra of SN 2021csp and SN 2019hgp (Type Icn) and of SN 2019uo and SN 2010al (Type Ibn). Both Type Ibn and Icn supernovae show narrow P-Cygni features in their early spectra, but the strengths of these transitions are much stronger in the Type Icn spectra to date.

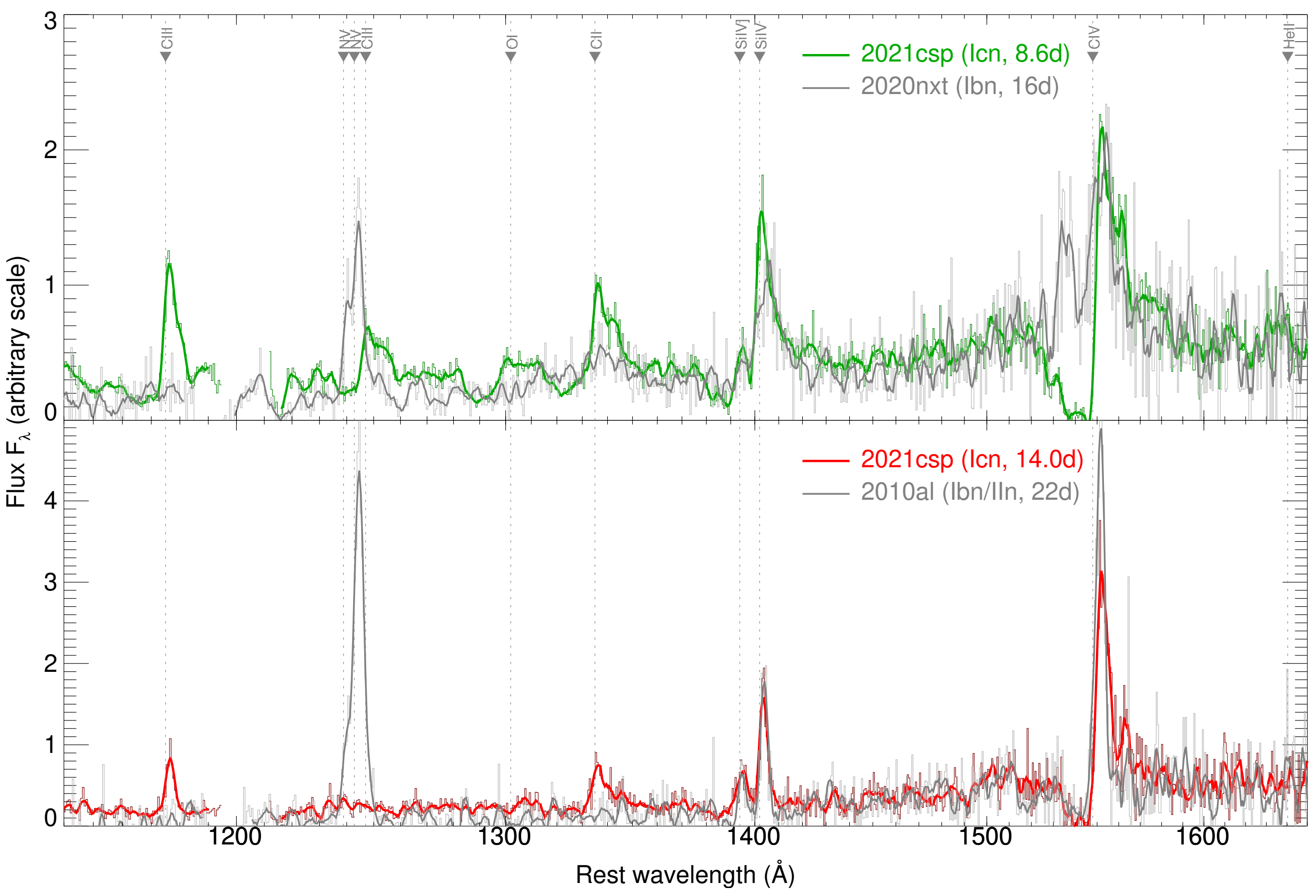

Figure 12. UV spectra of SN 2021cp compared to those of two Type Ibn SNe. The early spectrum of SN 2021csp is compared to the Type Ibn SN 2020nxt (Fox et al., in prep); the later spectrum is compared to the (later-phase) observation of Type Ibn SN 2010al (Kirshner et al. 2010).

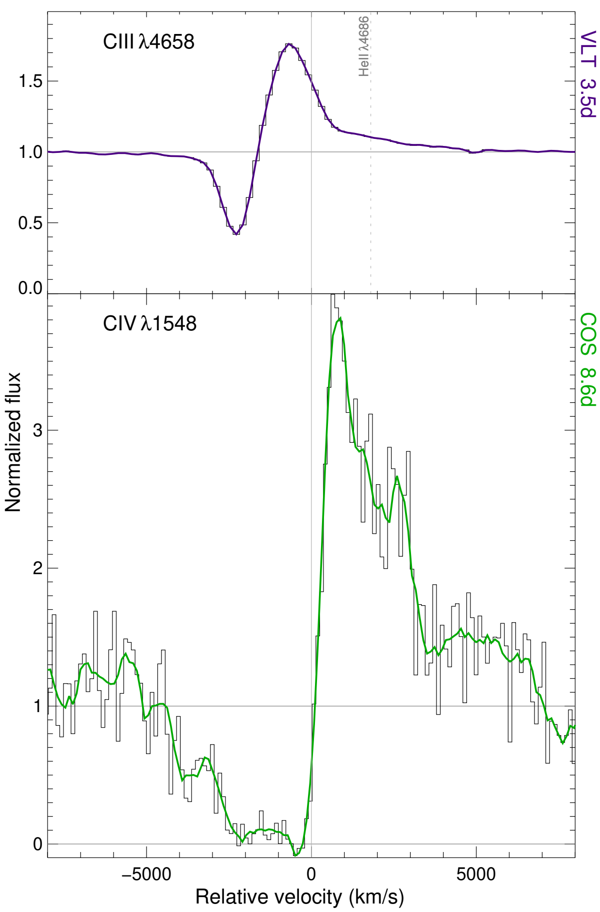

Figure 13. Line profiles for strong features in the optical and ultraviolet. The strongest absorption is seen with a net blueshift of approximately $v = -2200$ km s^{-1}, with a violet edge at $v = -4500 \pm 500$ km s^{-1}. Redshifted emission is also seen out to similarly high velocities.

that of SNe Ibn. In H-burning massive stars, the CNO cycle continuously converts H to He but also converts most existing C and O to N; CNO-processed material is expected to have $X_N/X_C \gtrsim 10$ (Gamow 1943; Crowther 2007). In contrast, during the He-burning phase, He is converted to C and O via the triple-alpha process but N is simultaneously consumed by conversion to Mg and Ne, leaving it heavily depleted. The absence of detectable N in the ultraviolet provides evidence that by the time of explosion virtually the entire remaining star (including its surface, as revealed by the CSM) had undergone triple-α processing.

As noted by Gal-Yam et al. (2021), the velocities and abundance patterns in Ibn vs. Icn supernovae strongly parallel what is seen in WR (WN vs. WC) stars. This does not guarantee that the progenitors *are* WR stars similar to the ones seen in the Milky Way and nearby galaxies: indeed, in §4.2 we will discuss that the properties of the SN Ibn/Icn progenitor stars shortly before explosion must be quite different from known WR stars. However, these properties do suggest that the SN Ibn/Icn progenitors must share two essential characteristics with WR stars: surface abundance patterns from envelope stripping, and high-velocity mass loss.

4.2. *Dramatically enhanced pre-explosion mass loss*

The fast evolutionary timescale of this transient (a very fast rise, followed by a rapid decline) can only be practically explained by CSM interaction, for reasons explained in previous works on similarly rapid and luminous objects (e.g., Rest et al. 2018): the decline is too fast if radioactive decay of heavy elements is responsible for the heating, but the rise is too slow (and the peak too luminous) to be shock cooling of a supergiant envelope. Qualitatively this is consistent with the spectroscopically-inferred notion of a CSM-interacting transient, and indeed our early observations provide some of the most direct evidence yet that fast-rising blue transients (of all spectroscopic types) do indeed result from strong CSM interaction. However, the properties of the CSM are quite extreme for a WR wind.

The SN reaches a peak luminosity of $\sim 2 \times 10^{44}$ erg s^{-1} on a timescale of only three days, and over the course of the first 10 days (over which interaction is the only viable source of energy deposition) the radiative energy release is approximately 10^{50} erg. While this is only a few percent of the kinetic energy budget of a typical SN, a substantial CSM is required to decelerate the ejecta over this timescale.

For a supernova powered by CSM interaction the pre-SN mass-loss rate can be related to the observed bolometric luminosity in a simple way assuming basic physical principles (see also Smith 2017a). A star losing mass isotropically at a constant velocity $v_{\rm CSM}$ but potentially variable mass-loss rate $\dot{M}$ will produce a wind nebula with density profile $\rho(r) = \dot{M}/(4\pi r^2 v_{\rm CSM})$. The SN shock then expands into this nebula at $v_{\rm ej}$, sweeping up matter at a rate $dM/dt = v_{\rm ej}\rho r^2 = v_{\rm ej}\dot{M}/(4\pi v_{\rm CSM})$. In the SN shock frame, this matter is suddenly decelerated and its kinetic energy is converted to heat; and some fraction ϵ of is released as thermal radiation. Thus, the luminosity is related to the mass loss rate as:

$$L_{\rm bol} = \frac{1}{2}\epsilon \dot{M}\left(\frac{v_{\rm ej}^3}{v_{\rm CSM}}\right)$$

For a variable mass-loss rate, the SN luminosity at post-explosion time t probes the mass-loss rate at pre-explosion time $-t(v_{\rm ej}/v_{\rm CSM})$.

For SN 2021csp, we have $v_{\rm CSM} \sim 1500$ km s^{-1} (from early spectroscopy), and $v_{\rm ej} \sim 30000$ km s^{-1} (from pho-

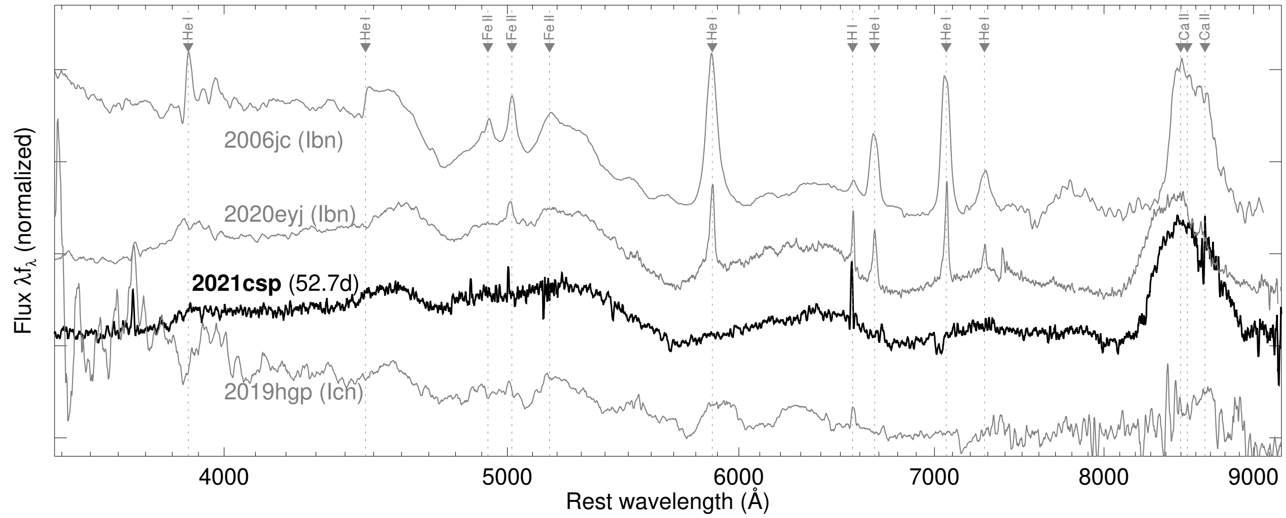

Figure 14. The late-time spectrum of SN 2021csp (from LRIS) compared to Type Icn SN 2019hgp (Gal-Yam et al. 2021) and two Type Ibn SNe (SN 2006jc from Pastorello et al. 2007 and SN 2020eyj from Kool et al., in prep).

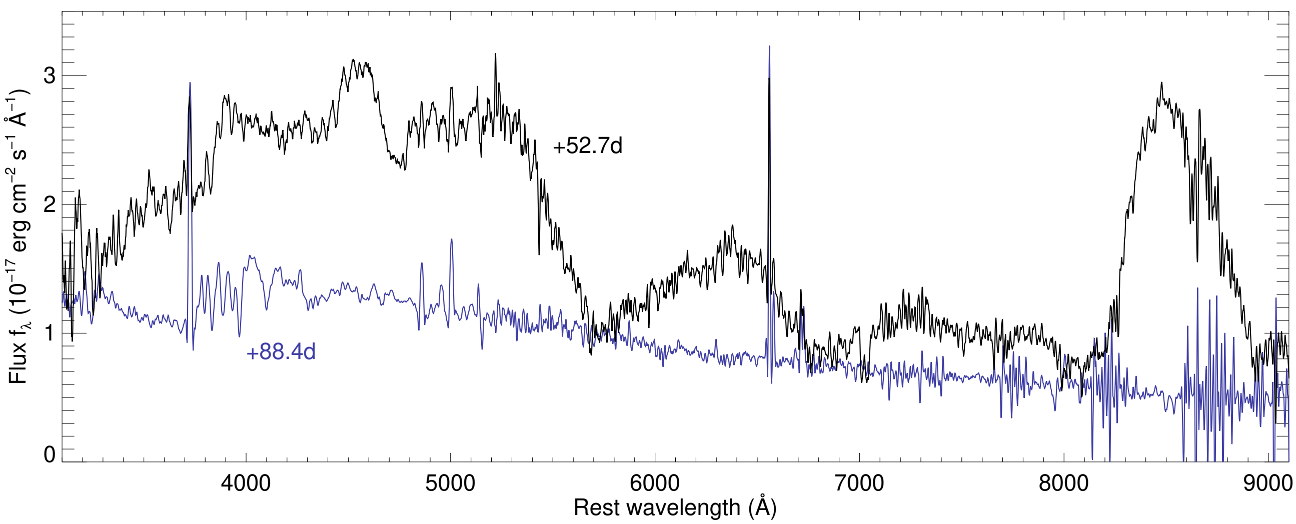

Figure 15. Late-phase spectroscopy of SN 2021csp. The upper spectrum (shown in black) was taken on 2021-04-14 and is still dominated by SN flux. The lower spectrum (in light brown) was taken a month later on 2021-05-16 at the same location and only host-galaxy features are evident.

tospheric modeling). For these parameters the mass-loss rate is:

$$\dot{M} = 0.18 \left(\frac{L}{10^{44}\ \mathrm{erg\,s^{-1}}} \right) \left(\frac{\epsilon}{0.1} \right)^{-1} M_\odot\,\mathrm{yr}^{-1}$$

Thus, at a time mapping to the bolometric peak of the light curve (+3 days post-explosion, or −60 days pre-explosion) the equivalent mass-loss rate of the star must have been close to 0.5 $M_\odot$ yr^{-1}. This is $\sim$ 4 orders of magnitude higher than what is seen in typical WR stars (e.g., Barlow et al. 1981; Smith 2017b)—or indeed any stars other than luminous blue variables (LBVs) undergoing giant eruptions.

The narrow lines largely disappear by 16 days, although we have reason to believe (§4.3) that interaction continues to be the dominant power source of the light curve over the remainder of the evolution of the SN. Under the simplistic assumptions above, the mass-loss rate 1 year prior to explosion was approximately 0.02 $M_\odot$ while three years prior to explosion it was 0.005 $M_\odot$, which is still a factor of 100 greater than for typical WR stars.

Based on this, we conclude that the dense and fast CSM indicated by our spectroscopy originates from a pre-explosion giant eruption rather than a WR wind. The very close separation in time between this eruption and the explosion (10^{-4} of the lifetime of the WR

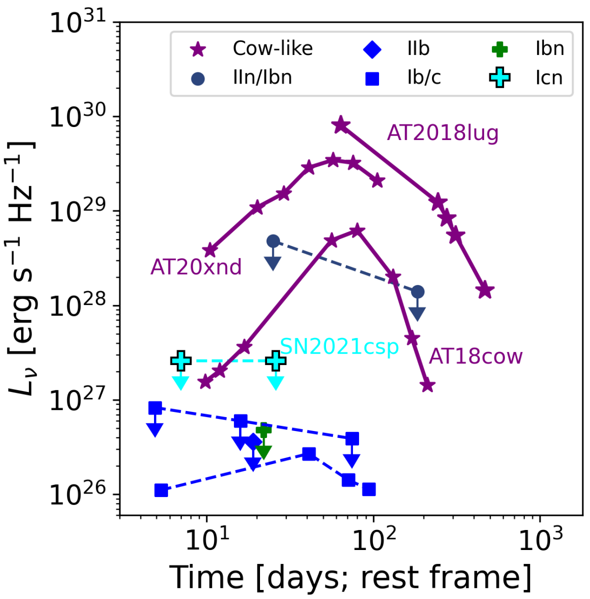

Figure 16. Radio luminosities versus those reported in Ho et al. (2021). A radio counterpart as bright as that seen in radio-loud FBOTs like AT 2021cow can be ruled out, but not a fainter source such as what was observed in the Type Ic-BL SN 2020bvc (Ho et al. 2020b).

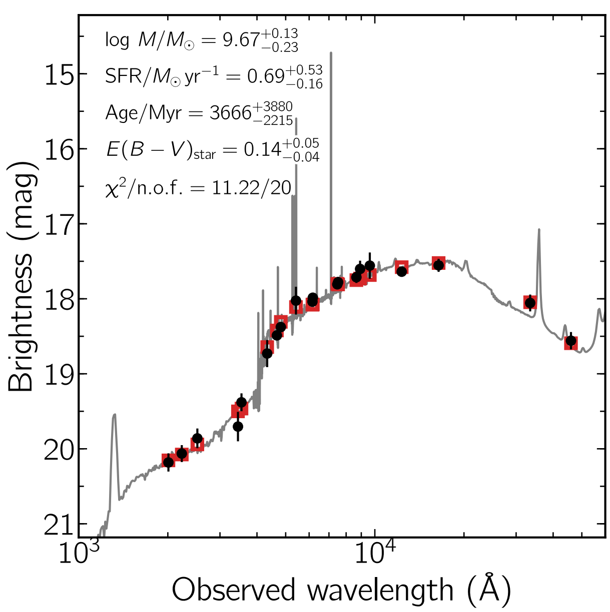

Figure 17. Spectral energy distribution (SED) of the host galaxy of SN 2021csp (black data points). The solid line displays the best-fitting model of the SED. The red squares represent the model-predicted magnitudes. The fitting parameters are shown in the upper-left corner. The abbreviation "n.o.f." stands for numbers of filters.

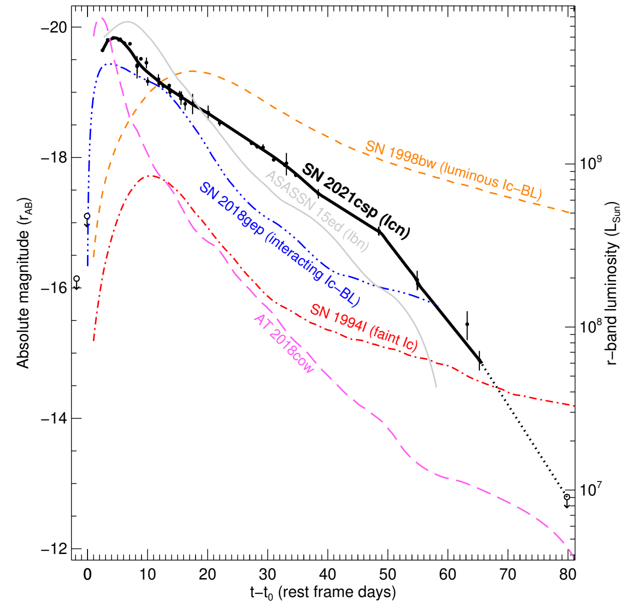

Figure 18. The optical (r-band) light curve of SN 2021csp as compared to several other transients likely arising from stripped-envelope stars: SN 1998bw (Patat et al. 2001; Clocchiatti et al. 2011), SN 2018gep (Ho et al. 2019a), SN 1994I (Richmond et al. 1996), ASASSN-15ed (Pastorello et al. 2015b), and AT 2018cow (Perley et al. 2019). The dotted segment is an extrapolation.

phase) is unlikely to be a coincidence and suggests that the star was undergoing a period of extreme instability, possibly brought on by late stages of nuclear burning, as has been inferred indirectly from observations of a variety of supernovae (Yaron et al. 2017; Bruch et al. 2021; Strotjohann et al. 2021) including at least one SN Ibn (Pastorello et al. 2007).

This is, however, not in contradiction to the notion that a WR star is responsible for the explosion. The light curves and spectra of SN 2021csp show that the interaction phase is very short-lived: once the zone of CSM originating from the pre-explosion eruption has been traversed by the shock, the interaction signatures disappear and the optical luminosity plummets, consistent with the explosion expanding into a more tenuous wind from that point onward. This behavior is quite different from Type IIn supernovae (which typically continue to interact with CSM for years) but similar to all but a few Type Ibn supernovae.

4.3. *A low radioactive mass*

While the spectra become dominated by broad ejecta features from 15 days and the luminosity remains high for several weeks thereafter, it is notable that the spectra during this phase do not resemble those of normal Type Ib/c supernovae: the identifiable features are mostly in emission (not absorption) and the "temperature" (a loose concept since the spectra no longer resemble a blackbody) remains high. Similar behavior is seen in Type Ibn supernovae, and can be interpreted as the consequence of an inversion of the usual temperature geometry: ejecta are being heated from the shock at the front (producing an emission-dominated spectrum), rather than from radioactive decay from beneath (responsible for the more typical absorption-dominated spectrum). The distinction from earlier phases is that the optical depth of the pre-shock material has dropped, and the photosphere has receded behind the shock (which may include swept-up CSM material).

This alone does not rule out the presence of radioactive heating as well: out to 60 days SN 2021csp is still quite luminous for a supernova and it is easy to imagine a "typical" SN Ic explosion buried behind the optically thick shock photosphere—as is generally presupposed (although rarely demonstrated) to exist in Type Ibn SNe. However, the late-time photometric limits provide strong constraints on radioactive heating.

Ordinary (non-interacting, non-superluminous) stripped envelope SNe exhibit two light curve phases: an optically-thick phase and an optically-thin phase. The optically-thick phase is powered primarily by the decay of ^{56}Ni to ^{56}Co and manifests as a gradual rise, peak, and decay; the characteristic timescale is set by the diffusion time within the ejecta but is typically about two weeks. The optically-thin phase is typically powered by the subsequent decay of ^{56}Co to ^{56}Fe and follows an exponential curve (linear in time-magnitude space) set by the half-life of ^{56}Co. The nickel-heated phase is not constrained by SN 2021csp, since it is overwhelmed by interaction, but the data strongly constrain the presence of a cobalt exponential-decay tail. Figure 18 plots the $r-$band light curve of SN 2021csp versus a number of other stripped envelope SNe, including the well-studied low-luminosity SN Ic 1994I. The light curve limit can be seen to fall well below even SN 1994I at late times, with demonstrating that SN 2021csp was quite ineffective at producing cobalt (and therefore nickel).

Using the empirical method of Hamuy (2003) to convert our late-time $r-$band limit to a constraint on the radioactive mass, we estimate $M_{\rm Ni} < 0.008 M_\odot$, which is lower than what has been inferred for virtually any well-studied Type Ic SN to date (Hamuy 2003; Anderson 2019; Afsariardchi et al. 2020). This method assumes gamma-ray trapping characteristic of other Type Ib/c supernovae, which may not be a good assumption if the ejecta mass is low. To account for this, we employ the gamma-ray trapping prescriptions from Clocchiatti & Wheeler (1997) and Sollerman et al. (1998) to calculate the r-band luminosity at 80 days for various combinations of $M_{\rm ej}$ and $M_{\rm Ni}$ and compare this with the limiting measurement. The result is plotted in Figure 19, with comparison objects from (Srivastav et al. 2014) and (Gagliano et al. 2021) shown in blue. Any explosion with properties consistent with previously observed non-interacting stripped-envelope supernovae is ruled out. A strong constraint on the radioactive mass ($M_{\rm Ni} < 0.03 M_\odot$) can be placed even if the ejecta mass is low. For ejecta masses characteristic of the successful explosion of a Wolf-Rayet star the limit is even stronger ($M_{\rm Ni} < 0.001 M_\odot$).

The luminosity from late-time cobalt decay could also be hidden by dust produced in the SN shock. Dust formation has been inferred at late times in at least one SN Ibn (Smith et al. 2008; Mattila et al. 2008) and has been appealed to as a partial explanation for the similarly faint late-time emission from that event. It is difficult to rule this scenario out entirely, as we lack late-time near-infrared photometry with which to search for dust emission that would be predicted in this scenario. However, newly-formed dust should not conceal the blue wings of the emission lines (which originate from material at the front of the ejecta). Our spectrum at 88 days shows no evidence for blueshifted Ca II emission, suggesting that the line did in fact intrinsically disappear. More generally, dust formation would have to be extremely rapid (progressing from virtually nonexistent at $\sim$50 days to $A_V > 2$ mag at 80 days) and the covering fraction would have to very high (>0.9). We therefore argue that dust formation is unlikely to explain the late-time rapid fading.

Regardless of the exact interpretation of the late-time observations, the implication is similar. The underlying explosion must have been underwhelming by supernova standards, expelling little matter and/or producing minimal radioactive elements in comparison to virtually any known non-interacting Type Ib/c supernova (but quite similar to the majority of Type Ibn supernovae). This, in turn, strongly suggests that Type Ibn/Icn events are *not* simply ordinary Type Ib/c SNe that happened to undergo enhanced mass loss prior to explosion: the underlying explosion must also be intrinsically different.

4.4. *Rate Constraints*

Type Icn SNe are clearly rare events: the first example was identified only in 2019 (SN 2019hgp presented by Gal-Yam et al. 2021) and the second in 2021 (SN 2021csp presented in this paper). Type Ibn SNe are not common either: only 38 are catalogued on the Transient Name Server as of this writing (June 2021), compared to 8700 Type Ia supernovae (which have similar peak luminosities and are detectable to similar distances). Naively

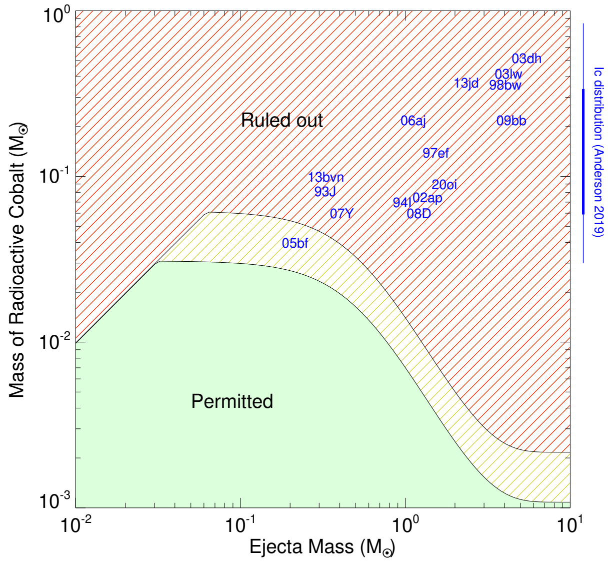

Figure 19. Constraints on the ejecta mass and the amount of radioactive nickel synthesized in the explosion as inferred from the deep late-time observation (assuming no self-obscuration). The "Permitted" region shows the part of parameter space consistent with the late-time NOT observation; the "Ruled Out" region shows parameter combinations that would predict optical emission inconsistent with the data (or with $M_{\rm Ni} < M_{\rm ej}$). The yellow intermediate region is the part of parameter space predicting a flux up to twice that observed, and may be permitted given uncertainties in the models. Comparison events from Srivastav et al. (2014) and Gagliano et al. (2021), and the distribution of Type Ic nickel masses from Anderson (2019), are also shown.

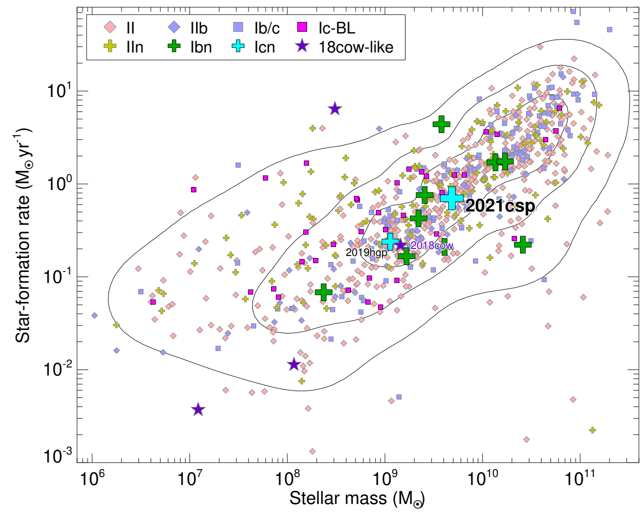

Figure 20. Host-galaxy stellar masses and star-formation rates for the iPTF sample of Schulze et al. (2020), compared to ZTF SN Icn and AT2018cow-like events. Much like the host of AT 2018cow, the host galaxy of SN 2021csp is a generally unremarkable intermediate-mass, star-forming galaxy. Contours from a kernel-density estimator of the iPTF sample are shown, enclosing approximately [50,80,95]% of the distribution.

this suggest that the SN Ibn rate is 0.4% of the SN Ia rate, with SN Icn rarer by at least a factor of 10. Given the relative SN Ia and core-collapse SN (CCSN) volumetric rates (e.g., Graur et al. 2011), this translates to ∼0.1% of all CCSNe being of Type Ibn and ∼0.01% of Type Icn.

This calculation neglects differences in the luminosity function and control times of the various events, as well as any bias in spectroscopic follow-up and reporting. A more robust limit can be calculated from the spectroscopically-complete ZTF Bright Transient Survey (Fremling et al. 2020; Perley et al. 2020). A detailed calculation of the volumetric rates of various CCSN subtypes from BTS will be presented in future work. For now, we use the methodology from Perley et al. (2020) (including new discoveries through summer 2021) to estimate the SN Ibn rate for peak absolute magnitudes brighter than −17.5 to be between 0.1%–0.5% of the total CCSN rate. If we assume that SNe Icn follow a similar luminosity distribution as SNe Ibn, the corresponding rate estimate for Type Icn SNe is approximately 0.005%–0.05%. Regardless of the precise numbers, the clear implication is that SNe Ibn/Icn are very rare explosions.

4.5. *An Intermediate-Mass Host Galaxy*

The integrated properties of the host galaxy are similar to those of the Large Magellanic Cloud and generally typical of star-forming galaxies. Figure 20 shows basic properties (mass and star-formation rate) compared to a variety of core-collapse SNe from the iPTF survey (Schulze et al. 2020); we have also plotted the four published AT 2018cow-like events with radio detections (Perley et al. 2019; Coppejans et al. 2020; Ho et al. 2020a; Lyman et al. 2020; Perley et al. 2021b) and SN 2019hgp (Gal-Yam et al. 2021). The host of SN 2021csp lies in the middle of the distribution on the star-forming main sequence. It is also well within the distributions of known Type Ibn and Type Ic-BL supernovae. Thus, for none of these classes is there strong evidence that a highly unusual (e.g., extremely metal-poor or ultra-massive) progenitor is required. Much larger samples of Type Icn (and Ibn) SNe will be needed to examine the implications for the nature of the progenitors in detail.

5. INTERPRETATION

To summarize, SN 2021csp represents the explosion of a H/He-depleted star into a CSM produced by rapid mass loss from the progenitor at very high velocities, likely in the form of an (unobserved) pre-explosion giant eruption. The explosion itself included a very fast ejecta component, yet synthesized relatively little nickel: the SN is dominated at all phases by features of the interaction. Deep limits at late times rule out a "classical" massive, slower-moving component to the ejecta, showing that the explosion did not simply originate from an ordinary class of SN exploding into enhanced CSM.

Qualitatively similar characteristics were noted for SN 2019hgp (Gal-Yam et al. 2021), and indeed for many of the prototypical Type Ibn supernovae as well. We consider here a few possible models for the observed behavior and the distinction from the general SN Ib/c population.

5.1. *A supernova from a highly stripped progenitor?*

A variety of faint-and-fast transients in recent years have been interpreted as the results of particularly effective stripping from the binary companion (De et al. 2018; McBrien et al. 2019; Yao et al. 2020). In this scenario, late-stage mass transfer is able to effectively remove the large majority of the mass of the progenitor star, leaving behind a core of only a few $M_{\odot}$ or less (Tauris et al. 2013). The explosion of such an object naturally produces a supernova with limited amounts of ejecta (including radioactive ejecta). Should such an explosion occur into a dense surrounding CSM shed by pre-explosion instabilities (not naturally predicted in these models, but plausible given the apparent ubiquity of enhanced late-stage mass loss in other SN classes), such behavior would be generally consistent with our observations of SN 2021csp and the population of Type Ibn/Icn transients more generally.

In this model, the strong similarities between Type Ibn/Icn SNe and WN/WC stars are not fundamental: the similar abundance patterns reflect common nucleosynthesis patterns more generally, while the similar velocities and line profiles would be largely coincidental. Binary evolution also provides a mechanism for maintaining a high rotation rate, which could produce a jet that may help in explaining the high photospheric velocities (§5.3).

A significant problem for this model is the fact that many Type Ibn SNe are not just rich in helium, but also retain significant amounts of hydrogen. Hydrogen is quite unlikely to persist in the progenitor of a star that has truly been heavily stripped. It is possible that Type Icn SNe do represent ultra-stripped stars while (some) Type Ibn SNe are produced by an entirely different mechanism, such as pulsational pair-instability (§5.2). However, if this is the case the strong similarities between the Type Ibn and Type Icn classes (in regards to timescale, luminosity, CSM velocity, and late-time behavior) must be ascribed almost entirely to coincidence given the huge divergence between the two models.

Thus, while it is difficult to rule out such a model on a purely object-by-object basis, the overall picture of the population of fast/luminous interacting transients leads us to consider other potential models.

5.2. *A pulsational pair-instability eruption?*

Another potential explanation for the lack of of a late-time radioactive tail is a *non-terminal* eruption that expels only the outer envelope of the star, leaving the remainder intact. It is already clear from the CSM properties that the star underwent an energetic eruption in the very recent past. If the unstable state that led to that prior eruption subsequently produced a second, higher-velocity eruption, the collision between the two shells could in particular produce a quite luminous transient. It is unlikely that an ordinary, LBV-style eruption would be sufficient for this, but a more exotic model might be sufficient: in particular, late-stage pulsational pair-instability models have been shown to reasonably reproduce the light curves of Type Ibn SNe (Woosley 2017; Karamehmetoglu et al. 2021).

We again disfavor this model, for several reasons. First, the pair-instability model has difficulty explaining the extremely high velocities inferred for SN 2021csp: both at early times (from the spectroscopy and blackbody modeling) but also at later phases (from the widths of the broad components in our last few spectra). Second, the host environments of Type Ibn and Icn supernovae are not generally consistent with the expectation that pair-instability supernovae should occur primarily or exclusively in extremely metal-poor environments. Finally, the complete absence of hydrogen (and strong depletion of helium) in Type Icn SNe is not a natural prediction of PPISN models.

5.3. *Jet Launching from a Failed Explosion of a WR Star?*

The third possibility is that the progenitor of SN 2021csp (and other Type Ibn/Icn supernovae) really is a massive Wolf-Rayet star undergoing core-collapse, but the supernova explosion was extraordinarily weak.

In general, one would expect more massive progenitors to produce explosions that are both more luminous (due to the larger cores) and slower-evolving (due to the more massive ejecta). There is some evidence that this is the case among "normal" Type II supernovae (Fraser et al. 2011) with identified progenitors. However, this trend is unlikely to extend to the highest masses: supernova simulations suggest that above a certain mass the shock should stall, causing most or all of the star to collapse to form a black hole (O'Connor & Ott 2011; Woosley & Heger 2015). The lowest-luminosity Type IIP supernovae have sometimes been attributed to marginally successful explosions suffering from substantial fallback (Zampieri et al. 2003), and it conceivable that Ibn/Icn SNe represent equivalent members of the stripped-envelope population.

The ejecta velocities inferred from the early-time modeling of SN 2021csp are extremely high, quite unlike what would be expected from a marginally-successful explosions. This suggests significant asymmetry, which could be produced if the explosion is driven by a jet. There is ample precedent to expect jet formation from WR stars collapsing to form black holes: the original "collapsar" model for gamma-ray bursts in which a rapidly-rotating compact object accelerates ultra-relativistic jets is the most famous (Woosley 1993), but more modest jet energies and velocities can be produced under less extreme conditions (MacFadyen et al. 2001; Piran et al. 2019). The interaction between a low-energy jet (or jet cocoon) and a dense shell of inner CSM could lead to a fast, but short-lived, interaction-driven transient of the type seen in SN 2021csp even as the bulk of the star collapses silently to a black hole. Spectropolarimetry (§2.3.4) does not suggest a highly asymmetric photosphere, but this could potentially be explained if the jet itself is hidden behind a quasi-spherical interaction shock.

It should be emphasized that in this model (or in any model), SN Ibn/Icn cannot represent the *typical* deaths of WR stars. Given the abundance of WR stars in the Local Group (Hainich et al. 2014; Rosslowe & Crowther 2015) and a lifetime of 10^6 years in this phase (Smith 2014), the predicted WR death rate is between 3–20% of the CCSN rate (Maoz & Badenes 2010), at least an order of magnitude in excess of what we inferred in §4.4. This should not be surprising: the extreme properties inferred from the early-phase observations of SN 2021csp and similar events require particularly extreme pre-explosion mass loss that may in practice be quite rare. In this scenario, the collapse of a high-mass star would generally produce only a relatively weak transient—consistent with the lack of good candidates for high-mass progenitors among the general SN Ib/c population—but in rare instances (perhaps 1% of the time) the explosion encounters dense surrounding CSM, leading to a fast-evolving and luminous transient.

6. CONCLUSIONS

SN 2021csp, the second example of the Type Icn supernova class to be discovered, is one of the most extreme examples of a interaction-powered fast and luminous transient to date and also among the best observed. Its properties, alongside those of SN 2019hgp (the first Icn) and the general population of Type Ibn supernovae, provide a challenge to the basic picture of interaction-driven supernovae as resulting from the explosions of otherwise ordinary SNe into dense CSM. The expansion speeds inferred from modeling the rising light curve are much higher than seen in ordinary stripped-envelope supernovae, while the late-time flux is far too faint for an explosion that produces significant ejecta and/or leads to significant radioactive nuclosynthesis (absent very rapid and extensive dust formation).

While the properties of SN 2021csp and other interacting SNe can be explained by a variety of potential models on an individual basis, the collective properties of this class points towards a scenario in which Type Ibn/Icn SNe are produced by partially-successful explosions following the collapse of massive Wolf-Rayet stars. Specifically, we propose a model in which the direct collapse of a WR star to a black hole launches a sub-relativistic jet that interacts with dense CSM shed by the progenitor shortly before explosion.

It is interesting to note that the one class of successful SNe for which modeling does suggest a significant contribution from high-mass progenitors (Type Ic-BL SNe; Taddia et al. 2019) has also been connected to jets and engines. The primary difference is that the vastly more powerful jets in those events produce far more luminous transients and supernova explosions and thus do not require dense CSM to be visible. However, there is increasing evidence that some SNe Ic-BL do interact with dense surrounding material as well (Corsi et al. 2014; Chen et al. 2018; Ho et al. 2020b), raising the possibility of a continuum of WR collapse transients, with the vast range in observable properties explained by variations in the jet power, pre-explosion mass loss history, and degree of progenitor stripping.

If this is the correct model, it would shed significant light on the even rarer, even faster-evolving transient population of AT2018cow-like transients, which show a number of similarities to Type Ibn/Icn SNe (Fox & Smith 2019). AT2018cow and its analogs have also been hypothesized (Perley et al. 2019; Margutti et al. 2019) to originate from "failed" collapses based on some of the same arguments presented above: the luminous early transient implies a very fast-moving early component, yet late-time observations provide deep limits on nickel production from the associated supernova, demonstrating that they cannot simply represent normal (or even rare) SNe exploding into an unusually dense medium. Cow-like transients show major differences from the SN

Ibn/Icn population, including a complete lack of early interaction signatures and a radio/X-ray "afterglow" that is more luminous than the limits on SNe Ibn/Icn by many orders of magnitude (Ho et al. 2019b, 2020a). This difference may be explicable in terms of the relative power and velocity of the jet and the precise geometry of the CSM, or it may be more fundamental.

Further studies will be necessary to resolve these questions. Even the Type Ibn population is only crudely mapped out, with sparingly few pre-max detections or deep late-time limits. SN 2021csp represents one of only two published Type Icn supernovae, and fewer than five spectroscopically-confirmed AT2018cow-like events are known. Fortunately, with ZTF and a number of other wide-area surveys fully operating and with increasing community interest in the fastest transients, the sample is destined to grow (albeit slowly) in the coming years.

The Legacy Survey of Space and Time (LSST) at Rubin Observatory will also play a vital role in this effort. While the slow cadence of the primary survey is poorly suited to the discovery of fast-evolving transients, photometric redshift constraints will make it far more straightforward to distinguish luminous phenomena in high-cadence shallower surveys, providing important synergy with the fast wide-field surveys of the future. Meanwhile, repeated deep LSST imaging of nearby galaxies may be able to test whether WR stars disappear without a trace, better seek out pre-explosion progenitor eruptions in future Type Ibn/Icn (and other) SNe, and search for dimmer transients associated with black hole fallback even in the absence of strong CSM interaction.

Based on observations obtained with the Samuel Oschin Telescope 48-inch and the 60-inch Telescope at the Palomar Observatory as part of the Zwicky Transient Facility project. ZTF is supported by the National Science Foundation under Grant No. AST-2034437 and a collaboration including Caltech, IPAC, the Weizmann Institute for Science, the Oskar Klein Center at Stockholm University, the University of Maryland, Deutsches Elektronen-Synchrotron and Humboldt University, the TANGO Consortium of Taiwan, the University of Wisconsin at Milwaukee, Trinity College Dublin, Lawrence Livermore National Laboratories, and IN2P3, France. Operations are conducted by COO, IPAC, and UW. SED Machine is based upon work supported by the National Science Foundation under Grant No. 1106171. The ZTF forced-photometry service was funded under the Heising-Simons Foundation grant #12540303 (PI: Graham). The Liverpool Telescope is operated on the island of La Palma by Liverpool John Moores University in the Spanish Observatorio del Roque de los Muchachos of the Instituto de Astrofisica de Canarias with financial support from the UK Science and Technology Facilities Council. The SED Machine is based upon work supported by the National Science Foundation under Grant No. 1106171. Partly based on observations made with the Nordic Optical Telescope, owned in collaboration by the University of Turku and Aarhus University, and operated jointly by Aarhus University, the University of Turku and the University of Oslo, representing Denmark, Finland and Norway, the University of Iceland and Stockholm University at the Observatorio del Roque de los Muchachos, La Palma, Spain, of the Instituto de Astrofisica de Canarias. These data were obtained with ALFOSC, which is provided by the Instituto de Astrofisica de Andalucia (IAA) under a joint agreement with the University of Copenhagen and NOT. Based on observations collected at the European Organisation for Astronomical Research in the Southern Hemisphere under ESO programme(s) 106.21U2 and 106.216C. J.S. and S.S. acknowledge support from the G.R.E.A.T. research environment funded by *Vetenskapsrådet*, the Swedish Research Council, under project number 2016-06012. OKC participation in ZTF was made available by the K.A.W. foundation.

MMK acknowledges generous support from the David and Lucille Packard Foundation. The GROWTH Marshal (Kasliwal et al. 2019) development was supported by the GROWTH project funded by the National Science Foundation under Grant No 1545949. IRAF is distributed by the National Optical Astronomy Observatories, which are operated by the Association of Universities for Research in Astronomy, Inc., under cooperative agreement with the National Science Foundation.

Facilities: HST(STIS,COS), Swift(XRT,UVOT), PO:1.2m(ZTF), PO:1.5m(SEDM), Hale(DBSP), LT(IO:O,SPRAT), VLA, Gemini:Gillett, NOT, VLT:Kueyen, Shane, Keck:I (LRIS)

Software: IRAF, Pypeit, LPipe, DBSP-DRP

REFERENCES

2021, DBSP-DRP, GitHub. https://github.com/finagle29/dbsp_drp

Afsariardchi, N., Drout, M. R., Khatami, D., et al. 2020, arXiv e-prints, arXiv:2009.06683. https://arxiv.org/abs/2009.06683

Ahn, C. P., Alexandroff, R., Allende Prieto, C., et al. 2012, ApJS, 203, 21, doi: 10.1088/0067-0049/203/2/21

Anderson, J. P. 2019, A&A, 628, A7, doi: 10.1051/0004-6361/201935027

Asplund, M., Grevesse, N., Sauval, A. J., & Scott, P. 2009, ARA&A, 47, 481, doi: 10.1146/annurev.astro.46.060407.145222

Barlow, M. J., Smith, L. J., & Willis, A. J. 1981, MNRAS, 196, 101, doi: 10.1093/mnras/196.2.101

Bellm, E. C., Kulkarni, S. R., Graham, M. J., et al. 2019a, PASP, 131, 018002, doi: 10.1088/1538-3873/aaecbe

Bellm, E. C., Kulkarni, S. R., Barlow, T., et al. 2019b, PASP, 131, 068003, doi: 10.1088/1538-3873/ab0c2a

Blagorodnova, N., Neill, J. D., Walters, R., et al. 2018, PASP, 130, 035003, doi: 10.1088/1538-3873/aaa53f

Blanchard, P. K., Berger, E., Nicholl, M., & Villar, V. A. 2020, ApJ, 897, 114, doi: 10.3847/1538-4357/ab9638

Breeveld, A. A., Landsman, W., Holland, S. T., et al. 2011, in American Institute of Physics Conference Series, Vol. 1358, American Institute of Physics Conference Series, ed. J. E. McEnery, J. L. Racusin, & N. Gehrels, 373–376, doi: 10.1063/1.3621807

Bruch, R. J., Gal-Yam, A., Schulze, S., et al. 2021, ApJ, 912, 46, doi: 10.3847/1538-4357/abef05

Burrows, D. N., Hill, J. E., Nousek, J. A., et al. 2005, SSRv, 120, 165, doi: 10.1007/s11214-005-5097-2

Calzetti, D., Armus, L., Bohlin, R. C., et al. 2000, ApJ, 533, 682, doi: 10.1086/308692

Cao, Y., Kasliwal, M. M., Arcavi, I., et al. 2013, ApJL, 775, L7, doi: 10.1088/2041-8205/775/1/L7

Cenko, S. B., Fox, D. B., Moon, D.-S., et al. 2006, PASP, 118, 1396, doi: 10.1086/508366

Chabrier, G. 2003, PASP, 115, 763, doi: 10.1086/376392

Chen, T. W., Inserra, C., Fraser, M., et al. 2018, ApJL, 867, L31, doi: 10.3847/2041-8213/aaeb2e

Chugai, N. N. 2009, MNRAS, 400, 866, doi: 10.1111/j.1365-2966.2009.15506.x

Cikota, A., Patat, F., Cikota, S., & Faran, T. 2017, MNRAS, 464, 4146, doi: 10.1093/mnras/stw2545

Clocchiatti, A., Suntzeff, N. B., Covarrubias, R., & Candia, P. 2011, AJ, 141, 163, doi: 10.1088/0004-6256/141/5/163

Clocchiatti, A., & Wheeler, J. C. 1997, ApJ, 491, 375, doi: 10.1086/304961

Coppejans, D. L., Margutti, R., Terreran, G., et al. 2020, ApJL, 895, L23, doi: 10.3847/2041-8213/ab8cc7

Corsi, A., Ofek, E. O., Gal-Yam, A., et al. 2014, ApJ, 782, 42, doi: 10.1088/0004-637X/782/1/42

Crowther, P. A. 2007, ARA&A, 45, 177, doi: 10.1146/annurev.astro.45.051806.110615

De, K., Kasliwal, M. M., Ofek, E. O., et al. 2018, Science, 362, 201, doi: 10.1126/science.aas8693

Dekany, R., Smith, R. M., Riddle, R., et al. 2020, PASP, 132, 038001, doi: 10.1088/1538-3873/ab4ca2

Dessart, L., Hillier, D. J., Li, C., & Woosley, S. 2012, MNRAS, 424, 2139, doi: 10.1111/j.1365-2966.2012.21374.x

Drout, M. R., Chornock, R., Soderberg, A. M., et al. 2014, ApJ, 794, 23, doi: 10.1088/0004-637X/794/1/23

Duev, D. A., Mahabal, A., Masci, F. J., et al. 2019, MNRAS, 489, 3582, doi: 10.1093/mnras/stz2357

Eldridge, J. J., Fraser, M., Smartt, S. J., Maund, J. R., & Crockett, R. M. 2013, MNRAS, 436, 774, doi: 10.1093/mnras/stt1612

Eldridge, J. J., & Maund, J. R. 2016, MNRAS, 461, L117, doi: 10.1093/mnrasl/slw099

Evans, P. A., Beardmore, A. P., Page, K. L., et al. 2007, A&A, 469, 379, doi: 10.1051/0004-6361:20077530

—. 2009, MNRAS, 397, 1177, doi: 10.1111/j.1365-2966.2009.14913.x

Filippenko, A. V. 1982, PASP, 94, 715, doi: 10.1086/131052

Fitzpatrick, E. L. 1999, PASP, 111, 63, doi: 10.1086/316293

Foley, R. J., Smith, N., Ganeshalingam, M., et al. 2007, ApJL, 657, L105, doi: 10.1086/513145

Fox, O. D., & Smith, N. 2019, MNRAS, 488, 3772, doi: 10.1093/mnras/stz1925

Fraser, M., Ergon, M., Eldridge, J. J., et al. 2011, MNRAS, 417, 1417, doi: 10.1111/j.1365-2966.2011.19370.x

Fremling, C., Dugas, A., & Sharma, Y. 2019, Transient Name Server Classification Report, 2019-188, 1

Fremling, C., Sollerman, J., Taddia, F., et al. 2016, A&A, 593, A68, doi: 10.1051/0004-6361/201628275

Fremling, C., Miller, A. A., Sharma, Y., et al. 2020, ApJ, 895, 32, doi: 10.3847/1538-4357/ab8943

Gagliano, A., Izzo, L., Kilpatrick, C. D., et al. 2021, arXiv e-prints, arXiv:2105.09963. https://arxiv.org/abs/2105.09963

Gal-Yam, A., Bruch, R., Schulze, S., et al. 2021, Nature, submitted

Gamow, G. 1943, ApJ, 98, 500, doi: 10.1086/144581

Gehrels, N., Chincarini, G., Giommi, P., et al. 2004, ApJ, 611, 1005, doi: 10.1086/422091

Graham, M. J., Kulkarni, S. R., Bellm, E. C., et al. 2019, PASP, 131, 078001, doi: 10.1088/1538-3873/ab006c

Graur, O., Poznanski, D., Maoz, D., et al. 2011, MNRAS, 417, 916, doi: 10.1111/j.1365-2966.2011.19287.x

Hainich, R., Rühling, U., Todt, H., et al. 2014, A&A, 565, A27, doi: 10.1051/0004-6361/201322696

Hamuy, M. 2003, ApJ, 582, 905, doi: 10.1086/344689

HI4PI Collaboration, Ben Bekhti, N., Flöer, L., et al. 2016, A&A, 594, A116, doi: 10.1051/0004-6361/201629178

Ho, A. Y. Q., Goldstein, D. A., Schulze, S., et al. 2019a, ApJ, 887, 169, doi: 10.3847/1538-4357/ab55ec

Ho, A. Y. Q., Phinney, E. S., Ravi, V., et al. 2019b, ApJ, 871, 73, doi: 10.3847/1538-4357/aaf473

Ho, A. Y. Q., Perley, D. A., Kulkarni, S. R., et al. 2020a, ApJ, 895, 49, doi: 10.3847/1538-4357/ab8bcf

Ho, A. Y. Q., Kulkarni, S. R., Perley, D. A., et al. 2020b, ApJ, 902, 86, doi: 10.3847/1538-4357/aba630

Ho, A. Y. Q., Perley, D. A., Gal-Yam, A., et al. 2021, arXiv e-prints, arXiv:2105.08811. https://arxiv.org/abs/2105.08811

Höflich, P. 1991, A&A, 246, 481

Högbom, J. A. 1974, A&AS, 15, 417

Hook, I. M., Jørgensen, I., Allington-Smith, J. R., et al. 2004, PASP, 116, 425, doi: 10.1086/383624

Karamehmetoglu, E., Fransson, C., Sollerman, J., et al. 2021, A&A, 649, A163, doi: 10.1051/0004-6361/201936308

Kasliwal, M. M., Cannella, C., Bagdasaryan, A., et al. 2019, PASP, 131, 038003, doi: 10.1088/1538-3873/aafbc2

Kilpatrick, C. D., Takaro, T., Foley, R. J., et al. 2018, MNRAS, 480, 2072, doi: 10.1093/mnras/sty2022

Kilpatrick, C. D., Drout, M. R., Auchettl, K., et al. 2021, MNRAS, 504, 2073, doi: 10.1093/mnras/stab838

Kirshner, R., Blondin, S., Chevalier, R., et al. 2010, The Astronomer's Telegram, 2513, 1

Lang, D. 2014, AJ, 147, 108, doi: 10.1088/0004-6256/147/5/108

Lawrence, A., Warren, S. J., Almaini, O., et al. 2007, MNRAS, 379, 1599, doi: 10.1111/j.1365-2966.2007.12040.x

Leja, J., Johnson, B. D., Conroy, C., van Dokkum, P. G., & Byler, N. 2017, ApJ, 837, 170, doi: 10.3847/1538-4357/aa5ffe

Li, C., Hillier, D. J., & Dessart, L. 2012, MNRAS, 426, 1671, doi: 10.1111/j.1365-2966.2012.21198.x

Lyman, J. D., Galbany, L., Sánchez, S. F., et al. 2020, MNRAS, 495, 992, doi: 10.1093/mnras/staa1243

MacFadyen, A. I., Woosley, S. E., & Heger, A. 2001, ApJ, 550, 410, doi: 10.1086/319698

Mahabal, A., Rebbapragada, U., Walters, R., et al. 2019, PASP, 131, 038002, doi: 10.1088/1538-3873/aaf3fa

Mainzer, A., Bauer, J., Cutri, R. M., et al. 2014, ApJ, 792, 30, doi: 10.1088/0004-637X/792/1/30

Maoz, D., & Badenes, C. 2010, MNRAS, 407, 1314, doi: 10.1111/j.1365-2966.2010.16988.x

Margutti, R., Metzger, B. D., Chornock, R., et al. 2019, ApJ, 872, 18, doi: 10.3847/1538-4357/aafa01

Marino, R. A., Rosales-Ortega, F. F., Sánchez, S. F., et al. 2013, A&A, 559, A114, doi: 10.1051/0004-6361/201321956

Masci, F. J., Laher, R. R., Rusholme, B., et al. 2019, PASP, 131, 018003, doi: 10.1088/1538-3873/aae8ac

Mattila, S., Meikle, W. P. S., Lundqvist, P., et al. 2008, MNRAS, 389, 141, doi: 10.1111/j.1365-2966.2008.13516.x

Mauerhan, J. C., Smith, N., Filippenko, A. V., et al. 2013, MNRAS, 430, 1801, doi: 10.1093/mnras/stt009

Maund, J. R., Wheeler, J. C., Patat, F., et al. 2007, MNRAS, 381, 201, doi: 10.1111/j.1365-2966.2007.12230.x

McBrien, O. R., Smartt, S. J., Chen, T.-W., et al. 2019, ApJL, 885, L23, doi: 10.3847/2041-8213/ab4dae

McMullin, J. P., Waters, B., Schiebel, D., Young, W., & Golap, K. 2007, in Astronomical Society of the Pacific Conference Series, Vol. 376, Astronomical Data Analysis Software and Systems XVI, ed. R. A. Shaw, F. Hill, & D. J. Bell (Astronomical Society of the Pacific), 127

Meisner, A. M., Lang, D., & Schlegel, D. J. 2017, AJ, 153, 38, doi: 10.3847/1538-3881/153/1/38

Miller, J. S., & Stone, R. P. S. 1993, in Lick Obs. Tech. Rep. 66.

Narayana Bhat, P., Meegan, C. A., von Kienlin, A., et al. 2016, ApJS, 223, 28, doi: 10.3847/0067-0049/223/2/28

Nicholl, M., Smartt, S. J., Jerkstrand, A., et al. 2015, MNRAS, 452, 3869, doi: 10.1093/mnras/stv1522

O'Connor, E., & Ott, C. D. 2011, ApJ, 730, 70, doi: 10.1088/0004-637X/730/2/70

Oke, J. B., & Gunn, J. E. 1982, PASP, 94, 586, doi: 10.1086/131027

Oke, J. B., Cohen, J. G., Carr, M., et al. 1995, PASP, 107, 375, doi: 10.1086/133562

Pastorello, A., Smartt, S. J., Mattila, S., et al. 2007, Nature, 447, 829, doi: 10.1038/nature05825

Pastorello, A., Mattila, S., Zampieri, L., et al. 2008, MNRAS, 389, 113, doi: 10.1111/j.1365-2966.2008.13602.x

Pastorello, A., Benetti, S., Brown, P. J., et al. 2015a, MNRAS, 449, 1921, doi: 10.1093/mnras/stu2745

Pastorello, A., Prieto, J. L., Elias-Rosa, N., et al. 2015b, MNRAS, 453, 3649, doi: 10.1093/mnras/stv1812

Patat, F., & Romaniello, M. 2006, PASP, 118, 146, doi: 10.1086/497581

Patat, F., Cappellaro, E., Danziger, J., et al. 2001, ApJ, 555, 900, doi: 10.1086/321526

Patterson, M. T., Bellm, E. C., Rusholme, B., et al. 2019, PASP, 131, 018001, doi: 10.1088/1538-3873/aae904

Peng, C. Y., Ho, L. C., Impey, C. D., & Rix, H.-W. 2002, AJ, 124, 266, doi: 10.1086/340952

—. 2010, AJ, 139, 2097, doi: 10.1088/0004-6256/139/6/2097

Perley, D., Yao, Y., Schulze, S., et al. 2021a, Transient Name Server AstroNote, 62, 1

Perley, D. A. 2019, PASP, 131, 084503, doi: 10.1088/1538-3873/ab215d

Perley, D. A., Mazzali, P. A., Yan, L., et al. 2019, MNRAS, 484, 1031, doi: 10.1093/mnras/sty3420

Perley, D. A., Fremling, C., Sollerman, J., et al. 2020, ApJ, 904, 35, doi: 10.3847/1538-4357/abbd98

Perley, D. A., Ho, A. Y. Q., Yao, Y., et al. 2021b, MNRAS (submitted), arXiv:2103.01968. https://arxiv.org/abs/2103.01968

Piascik, A. S., Steele, I. A., Bates, S. D., et al. 2014, in Society of Photo-Optical Instrumentation Engineers (SPIE) Conference Series, Vol. 9147, Proc. SPIE, 91478H, doi: 10.1117/12.2055117

Piran, T., Nakar, E., Mazzali, P., & Pian, E. 2019, ApJL, 871, L25, doi: 10.3847/2041-8213/aaffce

Prochaska, J., Hennawi, J., Westfall, K., et al. 2020, The Journal of Open Source Software, 5, 2308, doi: 10.21105/joss.02308

Pursiainen, M., Childress, M., Smith, M., et al. 2018, MNRAS, 481, 894, doi: 10.1093/mnras/sty2309

Rest, A., Garnavich, P. M., Khatami, D., et al. 2018, Nature Astronomy, 2, 307, doi: 10.1038/s41550-018-0423-2

Richmond, M. W., van Dyk, S. D., Ho, W., et al. 1996, AJ, 111, 327, doi: 10.1086/117785

Roming, P. W. A., Kennedy, T. E., Mason, K. O., et al. 2005, SSRv, 120, 95, doi: 10.1007/s11214-005-5095-4

Rosslowe, C. K., & Crowther, P. A. 2015, MNRAS, 447, 2322, doi: 10.1093/mnras/stu2525

Sana, H., de Mink, S. E., de Koter, A., et al. 2012, Science, 337, 444, doi: 10.1126/science.1223344

Sander, A. A. C., Hamann, W. R., Todt, H., et al. 2019, A&A, 621, A92, doi: 10.1051/0004-6361/201833712

Schlafly, E. F., & Finkbeiner, D. P. 2011, ApJ, 737, 103, doi: 10.1088/0004-637X/737/2/103

Schulze, S., Yaron, O., Sollerman, J., et al. 2020, arXiv e-prints, arXiv:2008.05988. https://arxiv.org/abs/2008.05988

Serkowski, K., Mathewson, D. S., & Ford, V. L. 1975, ApJ, 196, 261, doi: 10.1086/153410

Silverman, J. M., Foley, R. J., Filippenko, A. V., et al. 2012, MNRAS, 425, 1789, doi: 10.1111/j.1365-2966.2012.21270.x

Simmons, J. F. L., & Stewart, B. G. 1985, A&A, 142, 100

Smartt, S. J. 2009, ARA&A, 47, 63, doi: 10.1146/annurev-astro-082708-101737

—. 2015, PASA, 32, e016, doi: 10.1017/pasa.2015.17

Smith, N. 2014, ARA&A, 52, 487, doi: 10.1146/annurev-astro-081913-040025

—. 2017a, Interacting Supernovae: Types IIn and Ibn, ed. A. W. Alsabti & P. Murdin (Springer), 403, doi: 10.1007/978-3-319-21846-5_38

—. 2017b, Philosophical Transactions of the Royal Society of London Series A, 375, 20160268, doi: 10.1098/rsta.2016.0268

Smith, N., Foley, R. J., & Filippenko, A. V. 2008, ApJ, 680, 568, doi: 10.1086/587860

Smith, N., Li, W., Filippenko, A. V., & Chornock, R. 2011, MNRAS, 412, 1522, doi: 10.1111/j.1365-2966.2011.17229.x

Smith, N., Mauerhan, J. C., & Prieto, J. L. 2014, MNRAS, 438, 1191, doi: 10.1093/mnras/stt2269

Smith, N., Silverman, J. M., Chornock, R., et al. 2009, ApJ, 695, 1334, doi: 10.1088/0004-637X/695/2/1334

Sollerman, J., Cumming, R. J., & Lundqvist, P. 1998, ApJ, 493, 933, doi: 10.1086/305163

Srivastav, S., Anupama, G. C., & Sahu, D. K. 2014, MNRAS, 445, 1932, doi: 10.1093/mnras/stu1878

Steele, I. A., Smith, R. J., Rees, P. C., et al. 2004, in Society of Photo-Optical Instrumentation Engineers (SPIE) Conference Series, Vol. 5489, Proc. SPIE, ed. J. Oschmann, Jacobus M., 679–692, doi: 10.1117/12.551456

Strotjohann, N. L., Ofek, E. O., Gal-Yam, A., et al. 2021, ApJ, 907, 99, doi: 10.3847/1538-4357/abd032

Sukhbold, T., & Woosley, S. E. 2014, ApJ, 783, 10, doi: 10.1088/0004-637X/783/1/10

Taddia, F., Sollerman, J., Fremling, C., et al. 2019, A&A, 621, A71, doi: 10.1051/0004-6361/201834429

Tanaka, M., Tominaga, N., Morokuma, T., et al. 2016, ApJ, 819, 5, doi: 10.3847/0004-637X/819/1/5

Tauris, T. M., Langer, N., Moriya, T. J., et al. 2013, ApJL, 778, L23, doi: 10.1088/2041-8205/778/2/L23

Tody, D. 1986, in Society of Photo-Optical Instrumentation Engineers (SPIE) Conference Series, Vol. 627, Instrumentation in astronomy VI, ed. D. L. Crawford, 733, doi: 10.1117/12.968154

Vink, J. S., de Koter, A., & Lamers, H. J. G. L. M. 2001, A&A, 369, 574, doi: 10.1051/0004-6361:20010127

Wang, L., Wheeler, J. C., & Höflich, P. 1997, ApJL, 476, L27, doi: 10.1086/310495

Woosley, S. E. 1993, ApJ, 405, 273, doi: 10.1086/172359

—. 2017, ApJ, 836, 244, doi: 10.3847/1538-4357/836/2/244

Woosley, S. E., & Heger, A. 2015, The Deaths of Very Massive Stars, ed. J. S. Vink, Vol. 412 (Springer), 199, doi: 10.1007/978-3-319-09596-7_7

Wright, A. H., Robotham, A. S. G., Bourne, N., et al. 2016, MNRAS, 460, 765, doi: 10.1093/mnras/stw832

Wright, E. L., Eisenhardt, P. R. M., Mainzer, A. K., et al. 2010, AJ, 140, 1868, doi: 10.1088/0004-6256/140/6/1868

Yang, Y., Hoeflich, P., Baade, D., et al. 2020, ApJ, 902, 46, doi: 10.3847/1538-4357/aba759

Yao, Y., De, K., Kasliwal, M. M., et al. 2020, ApJ, 900, 46, doi: 10.3847/1538-4357/abaa3d

Yaron, O., Perley, D. A., Gal-Yam, A., et al. 2017, Nature Physics, 13, 510, doi: 10.1038/nphys4025

Zampieri, L., Pastorello, A., Turatto, M., et al. 2003, MNRAS, 338, 711, doi: 10.1046/j.1365-8711.2003.06082.x

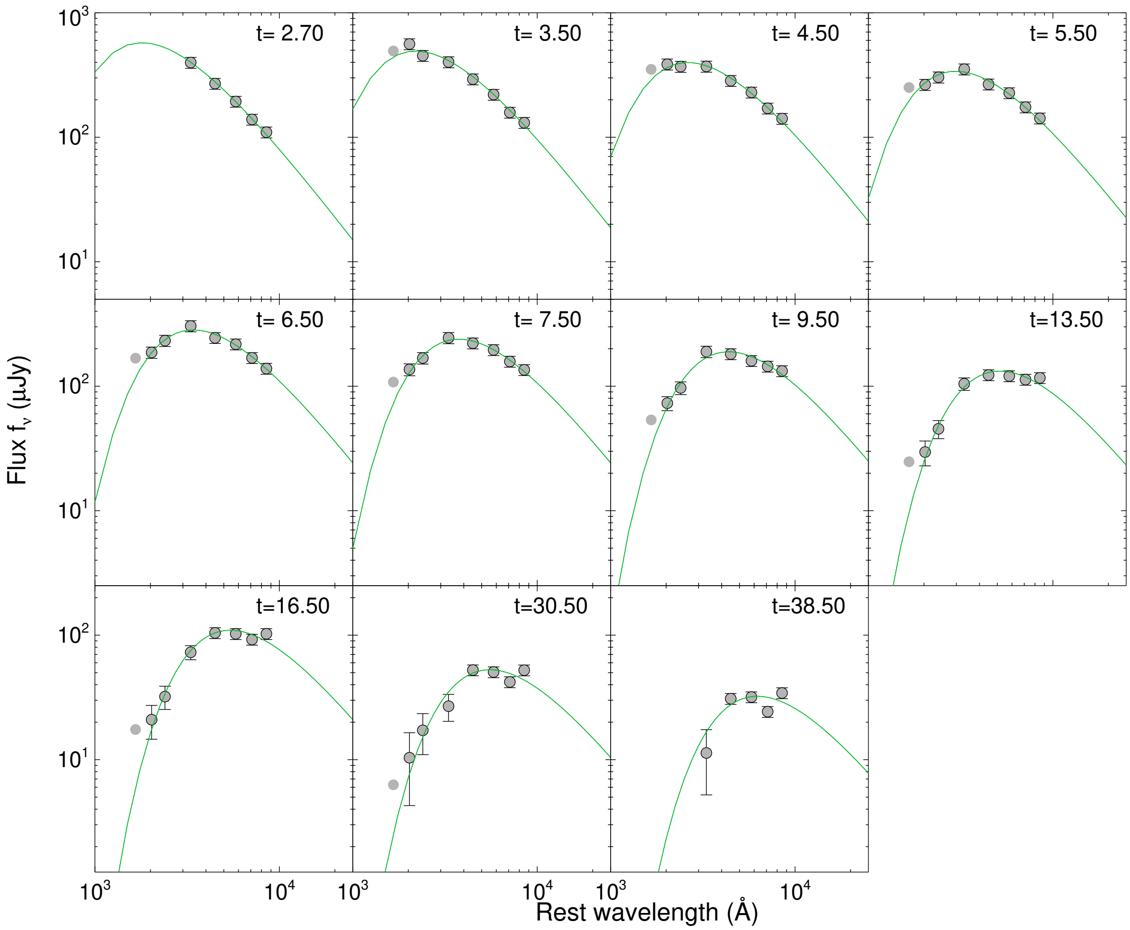

Figure 21. Blackbody fits to interpolated SEDs at various post-explosion times.

1759 APPENDIX

1760 .1. *Tables*

Table 1. SN 2021csp Photometry

Instrument	MJD (days)	Filter	AB Mag	unc.
P48	59250.4258	r	>21.09	
P48	59250.4648	g	>21.27	
P48	59252.4141	i	>20.72	
P48	59252.5195	r	>21.75	
P48	59254.4219	r	>20.79	
P48	59254.5273	g	>21.50	
P48	59256.4766	i	19.05	0.06
P48	59256.5078	g	18.11	0.02

Table 1 *continued*

Table 1 *(continued)*

Instrument	MJD (days)	Filter	AB Mag	unc.
LT	59257.1992	g	17.92	0.02
LT	59257.1992	r	18.25	0.02
LT	59257.2031	u	17.53	0.02
LT	59257.2031	i	18.59	0.02
LT	59257.2031	z	18.84	0.03
UVOT	59257.9570	W1	17.43	0.06
UVOT	59257.9688	W2	17.36	0.07
UVOT	59257.9766	M2	17.27	0.05
LT	59258.1367	g	17.82	0.02
LT	59258.1406	i	18.43	0.02
LT	59258.1406	u	17.52	0.03
LT	59258.1406	r	18.09	0.02
LT	59258.1445	z	18.62	0.05
LT	59259.1289	g	17.87	0.02
LT	59259.1289	r	18.06	0.02
LT	59259.1328	z	18.56	0.04
LT	59259.1328	u	17.62	0.02
LT	59259.1328	i	18.36	0.02
LT	59260.1680	r	18.09	0.02
LT	59260.1680	i	18.34	0.04
LT	59260.1680	g	17.95	0.02
LT	59260.1719	z	18.53	0.08
LT	59260.1719	u	17.63	0.04
P48	59260.4062	r	18.08	0.03
UVOT	59260.7539	W1	18.06	0.07
UVOT	59260.7617	W2	18.40	0.08
UVOT	59260.7656	M2	18.38	0.07
LT	59261.1562	g	18.04	0.02
LT	59261.1562	i	18.39	0.02
LT	59261.1562	r	18.14	0.02
LT	59261.1602	z	18.64	0.03
LT	59261.1602	u	17.87	0.02
UVOT	59261.4531	W1	18.24	0.09
UVOT	59261.4570	W2	18.71	0.09
UVOT	59261.4688	M2	18.67	0.07
LT	59262.1523	g	18.14	0.02
LT	59262.1562	u	18.13	0.04
LT	59262.1562	r	18.15	0.02
LT	59262.1562	i	18.44	0.04
LT	59262.1602	z	18.58	0.09
UVOT	59262.3750	W1	18.71	0.09
UVOT	59262.3828	W2	19.22	0.10
UVOT	59262.3867	M2	18.96	0.09
UVOT	59263.1719	W1	18.88	0.10
UVOT	59263.1836	W2	19.54	0.12

Table 1 *continued*

Table 1 *(continued)*

Instrument	MJD (days)	Filter	AB Mag	unc.
UVOT	59263.1914	M2	19.17	0.09
P48	59263.4375	r	18.50	0.16
P48	59263.4570	r	18.48	0.11
P48	59263.5195	g	18.32	0.03
LT	59264.1367	r	18.38	0.02
LT	59264.1367	g	18.36	0.02
LT	59264.1367	i	18.59	0.02
LT	59264.1406	u	18.38	0.09
LT	59264.1406	z	18.66	0.03
P48	59264.3945	i	18.61	0.05
UVOT	59264.6484	W1	19.22	0.18
LT	59265.1289	g	18.45	0.05
LT	59265.1289	i	18.52	0.08
LT	59265.1289	r	18.44	0.08
LT	59265.1328	u	18.31	0.08
LT	59265.1328	z	18.66	0.07
P48	59265.3594	r	18.73	0.06
P48	59265.4219	g	18.54	0.03
UVOT	59265.5977	W1	19.35	0.12
UVOT	59265.6055	W2	20.14	0.14
UVOT	59265.6094	M2	20.17	0.13
UVOT	59266.7852	W1	20.06	0.16
UVOT	59266.7930	W2	20.53	0.17
UVOT	59266.7969	M2	20.27	0.13
UVOT	59267.1875	W1	19.62	0.15
UVOT	59267.1953	W2	20.44	0.18
UVOT	59267.1992	M2	20.22	0.15
P60	59267.2969	r	18.69	0.08
P60	59267.3008	i	18.57	0.07
P60	59267.3008	g	18.60	0.07
P48	59267.3477	i	18.65	0.11
P48	59267.3789	g	18.76	0.06
P48	59267.4219	r	18.76	0.05
LT	59268.1836	g	18.76	0.02
LT	59268.1836	i	18.78	0.03
LT	59268.1836	r	18.80	0.02
LT	59268.1875	u	19.08	0.05
LT	59268.1875	z	18.79	0.04
LT	59269.1562	i	18.91	0.04
LT	59269.1562	r	18.83	0.04
LT	59269.1562	g	18.92	0.03
LT	59269.1602	z	18.82	0.04
LT	59269.1602	u	19.21	0.08
LT	59269.2383	r	18.79	0.02
LT	59269.2383	g	18.88	0.02

Table 1 *continued*

Table 1 *(continued)*

Instrument	MJD (days)	Filter	AB Mag	unc.
LT	59269.2422	u	19.19	0.04
LT	59269.2422	i	18.93	0.03
LT	59269.2461	z	18.82	0.04
P48	59269.3945	r	18.89	0.06
P48	59269.4570	g	18.79	0.05
P48	59270.4805	i	19.12	0.12
LT	59271.1289	g	18.98	0.08
LT	59271.1289	i	19.11	0.05
LT	59271.1289	r	18.92	0.05
LT	59271.1328	u	19.34	0.17
LT	59271.1367	z	18.93	0.08
P60	59271.3633	r	18.99	0.09
P60	59271.3672	i	18.73	0.07
P60	59271.3672	g	18.76	0.07
P48	59271.4219	g	18.82	0.10
P48	59271.4570	r	18.95	0.07
LT	59272.1133	g	18.94	0.05
LT	59272.1172	r	19.07	0.09
LT	59272.1172	i	18.90	0.08
LT	59272.1172	u	19.54	0.22
LT	59272.1211	z	18.97	0.07
UVOT	59272.6953	W1	20.55	0.21
UVOT	59272.6992	W2	21.21	0.25
UVOT	59272.7031	M2	20.88	0.18
P48	59273.3984	g	19.32	0.23
P48	59273.4609	r	19.06	0.14
UVOT	59273.6602	W1	20.66	0.24
UVOT	59273.6641	W2	21.23	0.26
UVOT	59273.6680	M2	21.48	0.36
LT	59276.2656	g	19.22	0.07
LT	59276.2695	i	19.51	0.18
LT	59276.2695	r	19.20	0.11
LT	59276.2734	z	18.87	0.12
P48	59278.3398	g	19.33	0.07
P60	59278.3516	g	19.33	0.03
P60	59278.3555	r	19.36	0.05
P60	59278.3594	i	19.25	0.07
UVOT	59279.7461	W2	22.17	0.55
UVOT	59279.7461	W1	20.43	0.24
UVOT	59279.7539	M2	21.49	0.32
P48	59280.3398	i	19.68	0.14
LT	59284.0977	g	19.61	0.04
LT	59284.0977	r	19.67	0.02
LT	59284.1016	i	19.78	0.04
LT	59284.1055	z	19.54	0.06

Table 1 *continued*

Table 1 *(continued)*

Instrument	MJD (days)	Filter	AB Mag	unc.
UVOT	59284.4883	W1	20.95	0.43
UVOT	59284.4922	W2	23.29	1.23
UVOT	59284.4922	M2	21.08	0.32
LT	59285.0781	g	19.74	0.04
LT	59285.0820	i	19.93	0.02
LT	59285.0820	r	19.72	0.04
LT	59285.0898	u	20.52	0.20
LT	59286.1680	g	19.74	0.02
LT	59286.1719	i	19.94	0.06
LT	59286.1719	r	19.74	0.05
LT	59286.1758	z	19.82	0.10
LT	59286.1797	u	20.49	0.23
UVOT	59286.5039	W1	22.17	0.60
UVOT	59286.5117	M2	22.08	0.39
UVOT	59286.5117	W2	22.09	0.45
LT	59288.0938	g	19.93	0.02
LT	59288.0977	r	19.93	0.02
LT	59288.0977	i	20.11	0.03
LT	59288.1016	z	19.90	0.06
LT	59288.1055	u	20.87	0.11
UVOT	59288.5391	W1	23.30	1.20
UVOT	59288.5469	W2	22.01	0.44
UVOT	59288.5508	M2	22.44	0.49
LT	59290.1016	g	20.04	0.02
LT	59290.1055	r	20.01	0.03
LT	59290.1055	i	20.28	0.09
LT	59290.1094	z	19.85	0.09
LT	59290.1133	u	21.12	0.15
P48	59290.3945	r	19.98	0.16
LT	59292.0898	g	20.20	0.05
LT	59292.0938	r	20.17	0.03
LT	59292.0977	i	20.49	0.04
LT	59292.0977	z	20.04	0.04
LT	59292.1094	u	21.28	0.10
LT	59296.1562	g	20.53	0.08
LT	59296.1602	i	20.72	0.10
LT	59296.1602	r	20.45	0.07
LT	59296.1641	z	20.27	0.09
LT	59296.1719	u	21.72	0.57
LT	59307.0156	g	20.98	0.11
LT	59307.0195	r	21.02	0.06
LT	59307.0234	i	21.44	0.12
LT	59307.0273	z	20.75	0.25
LT	59307.0352	u	22.39	1.12
NOT	59307.0938	r	21.02	0.07

Table 1 *continued*

Table 1 *(continued)*

Instrument	MJD (days)	Filter	AB Mag	unc.
NOT	59307.0977	g	21.07	0.05
NOT	59307.1016	i	21.49	0.07
LT	59312.0469	z	21.32	0.39
LT	59313.9922	g	21.63	0.07
LT	59314.0000	r	21.77	0.14
LT	59314.0078	i	21.87	0.15
LT	59314.1016	r	21.83	0.08
LT	59314.1055	i	22.28	0.17
NOT	59323.0273	r	22.45	0.20
NOT	59323.0352	g	22.40	0.20
NOT	59323.0430	i	22.80	0.20
NOT	59325.2227	r	23.00	0.14
NOT	59341.0352	r	>24.80	

Note—Table of photometry. Magnitudes are not corrected for Galactic extinction.

Table 2. Log of spectroscopy for SN 2021csp

Observation date (UTC)	MJD (days)	Phase (days)	Facility	Exp. time (s)	Grism/Grating	Slit width (arcsec)	Range (Å)
2021 Feb 12 04:23:54	59257.183	2.475	LT/SPRAT	2×600	Blue	1.8	4020–7994
2021 Feb 12 15:07:38	59257.630	2.888	Gemini/GMOS	2×900	B600	1.0	3641–6878
2021 Feb 13 05:36:01	59258.233	3.444	LT/SPRAT	2×600	Blue	1.8	4000–8000
2021 Feb 13 06:18:33	59258.263	3.471	NOT/ALFOSC	1800	Grism#4	1.0	3852–9681
2021 Feb 13 07:18:40	59258.305	3.510	VLT/FORS2	8×750	300V	1.0	4400–9200
2021 Feb 14 03:54:36	59259.163	4.302	LT/SPRAT	2×600	Blue	1.8	4000–8000
2021 Feb 15 03:30:05	59260.146	5.208	LT/SPRAT	2×600	Blue	1.8	4000–8000
2021 Feb 15 05:17:55	59260.221	5.277	NOT/ALFOSC	2×900	Grism#4	1.3	3501–9635
2021 Feb 16 04:40:52	59261.195	6.176	LT/SPRAT	2×600	Blue	1.8	4000–8000
2021 Feb 17 05:24:30	59262.225	7.127	NOT/ALFOSC	2×1800	Grism#4	1.3	3504–9635
2021 Feb 18 12:09:43	59263.507	8.309	HST/STIS	2100	G230L	0.2	1570–3180
2021 Feb 18 13:12:00	59263.550	8.349	Lick/KAST	xx	xx	xx	3632–10340
2021 Feb 18 20:05:29	59263.837	8.614	HST/COS	4243	G140L	–	1230–2050
2021 Feb 19 03:57:39	59264.165	8.916	LT/SPRAT	2×600	Blue	1.8	4000–8000
2021 Feb 20 02:16:36	59265.095	9.774	NOT/ALFOSC	2×1800	Grism#4	1.3	3501–9631
2021 Feb 22 01:58:28	59267.082	11.607	HST/STIS	2030	G230L	0.2	1570–3180
2021 Feb 23 05:15:11	59268.219	12.656	LT/SPRAT	2×600	Blue	1.8	4000–8000
2021 Feb 24 15:58:17	59269.665	13.990	HST/COS	4003	G140L	–	1230–2050
2021 Feb 27 02:19:35	59272.097	16.233	NOT/ALFOSC	2×1800	Grism#4	1.0	3753–9683
2021 Mar 09 05:19:36	59282.222	25.574	NOT/ALFOSC	2×1800	Grism#4	1.3	3752–9620
2021 Mar 16 03:18:45	59289.138	31.954	NOT/ALFOSC	3×1500	Grism#4	1.0	3701–9683
2021 Mar 23 01:48:34	59296.075	38.354	NOT/ALFOSC	3×1500	Grism#4	1.0	4001–9685
2021 Apr 03 02:42:56	59307.113	48.536	NOT/ALFOSC	3×1500	Grism#4	1.0	4003–9677
2021 Apr 07 14:32:41	59311.606	52.681	Keck/LRIS	2×755	B600+R400	1.0	3134–10284
2021 Apr 09 10:28:48	59313.437	54.370	Palomar/DBSP	1×1200	B600+R316	1.5	3400–10000
2021 Apr 14 11:32:20	59318.481	59.023	Keck/LRIS	1×450	B400+R400	1.0	3000–10306
2021 May 10 10:56:35	59344.456	82.985	Keck/LRIS	3×902	B400+R400	1.0	3000–10306
2021 May 16 07:52:14	59350.328	88.402	Keck/LRIS	3×902	B400+R400	1.0	3000–10306

Note—The phase is calculated with respect to MJD 59254.5 (the estimated explosion date) and is given in the rest frame.

Table 3. Photometry of the SN 2021csp host galaxy

Survey/ Telescope	Filter	Magnitude
Swift/UVOT	$uvw2$	20.52 ± 0.16
Swift/UVOT	$uvm2$	20.47 ± 0.07
Swift/UVOT	$uvw1$	20.08 ± 0.10
SDSS	u	19.51 ± 0.11
SDSS	g	18.59 ± 0.03
SDSS	r	18.11 ± 0.02
SDSS	i	17.86 ± 0.03
SDSS	z	17.64 ± 0.10
PS1	g	18.47 ± 0.04
PS1	r	18.06 ± 0.03
PS1	i	17.83 ± 0.05
PS1	z	17.75 ± 0.06
PS1	y	17.59 ± 0.17
UKIDSS	J	17.66 ± 0.03
UKIDSS	H	17.57 ± 0.07
WISE	$W1$	18.06 ± 0.05
WISE	$W2$	18.56 ± 0.06

Note—All magnitudes are reported in the AB system and not corrected for extinction.

Table 4. Results of blackbody modeling

MJD	t (d)	$\log_{10}(L)$ (erg s^{-1})	$\log_{10}(R)$ (cm)	$\log_{10}(T)$ (K)
59257.20	2.70	$44.33^{+0.18}_{-0.28}$	$14.88^{+0.10}_{-0.06}$	$4.45^{+0.07}_{-0.12}$
59258.00	3.50	$44.17^{+0.16}_{-0.02}$	$14.98^{+0.01}_{-0.07}$	$4.37^{+0.07}_{-0.01}$
59259.00	4.50	$44.00^{+0.04}_{-0.03}$	$15.06^{+0.02}_{-0.03}$	$4.28^{+0.02}_{-0.02}$
59260.00	5.50	$43.88^{+0.02}_{-0.04}$	$15.11^{+0.04}_{-0.01}$	$4.23^{+0.01}_{-0.03}$
59261.00	6.50	$43.74^{+0.03}_{-0.02}$	$15.15^{+0.03}_{-0.03}$	$4.18^{+0.02}_{-0.02}$
59262.00	7.50	$43.63^{+0.03}_{-0.02}$	$15.17^{+0.02}_{-0.02}$	$4.13^{+0.02}_{-0.02}$
59264.00	9.50	$43.46^{+0.02}_{-0.02}$	$15.21^{+0.03}_{-0.03}$	$4.07^{+0.02}_{-0.02}$
59268.00	13.50	$43.23^{+0.03}_{-0.02}$	$15.25^{+0.03}_{-0.03}$	$4.00^{+0.02}_{-0.01}$
59271.00	16.50	$43.13^{+0.03}_{-0.03}$	$15.25^{+0.03}_{-0.03}$	$3.97^{+0.02}_{-0.02}$
59285.00	30.50	$42.80^{+0.04}_{-0.04}$	$15.10^{+0.04}_{-0.04}$	$3.96^{+0.02}_{-0.02}$
59293.00	38.50	$42.55^{+0.05}_{-0.04}$	$15.04^{+0.06}_{-0.07}$	$3.93^{+0.04}_{-0.03}$

Note—Uncertainties are statistical only. The true uncertainties, particularly at late times, are likely to be larger.